DLR-Institut für Vernetzte Energiesysteme e.V.

Carl-von-Ossietzky Universität Oldenburg

Masterarbeit im Studiengang Chemie

Synthesis and Characterisation of Iron/Cobalt Bimetallic Me-N-C Catalysts for Electrochemical Oxygen Reduction

Erstgutachter: Prof. Dr. Michael Wark

Zweitgutachter: Dr. Alexander Dyck

Marius Gollasch

Oldenburg, 31. Januar 2020

Contents

List of Figures

Abbreviations and Symbols

Table of Abbreviations

AES	Auger-Electron Spectroscopy
AST	Accelerated Stress Test
BP_{ox}	Oxidised Black Pearls
BPP	Bipolar Plate
CE	Counter Electrode
CV	Cyclic Voltammetry
EDS	Energy Dispersive X-ray Spectroscopy
EIS	Electrochemical Impedance Spectroscopy
EXAFS	Extended X-ray Absorption Fine Structure
FCCJ	Fuel Cell Conference of Japan
FWHM	Full Width at Half Maximum
GDL	Gas Diffusion Layer
HOR	Hydrogen Oxidation Reaction
HR-TEM	High-Resolution TEM
HT	High-Temperature
iR	Internal Resistance
LT	Low-Temperature
MEA	Membrane Electrode Assembly
MOF	Metal Organic Framework
OCP	Open-Circuit Potential
ORR	Oxygen Reduction Reaction
PEM	Proton Exchange Membrane
PEMFC	Proton Exchange Membrane Fuel Cell
PTFE	Polytetrafluoroethylene
RE	Reference Electrode
RDE	Rotating Ring Electrode
RHE	Reversible Hydrogen Electrode
RRDE	Rotating Ring Disk Electrode

TEM	Transmission Electron Microscopy
WE	Working Electrode
XANES	X-ray Absorption Near Edge Structure
XPS	X-ray Photoelectron Spectroscopy
XRD	X-ray Diffraction

Table of Symbols

$E_{1/2}$	Half-wave Potential
j_{lim}	Diffusion Limited Current Density
j	Current Density
j_{kin}	Kinetic Current Density
E	Potential
N	RRDE Collection Efficiency
j_R	RRDE Ring Current Density
j_D	RRDE Disk Current Density
$X_{H_2O_2}$	H_2O_2 Yield
E_{kin}	Kinetic Energy
$h\nu$	Electromagnetic Radiation Energy
Θ_s	Spectrometer Workfunction
E_B	Binding Energy
$\lambda(E)$	Electron Inelastic Mean Free Path
s	Spin Quantum Number
l	Angular Momentum Quantum Number
J	Total Angular Momentum Quantum Number
n	Principal Quantum Number
I_i	XPS Signal Intensity
L_i	Photon Flux
c_i	Concentration of the Element
σ_i	Photon Ionisation Area or Scofield Factor
K	XPS Instrument Specific Constant
$\lambda(E)_i$	Electron Attenuation Length
S	XPS Sensitivity Factor
λ	Wavelength
θ	Glancing Angle
Δ	Path-length Difference
d	Lattice Separation
Z''	Real Part of the Complex Impedance
U_{corr}	Corrected Potential

I	Current
R_{Ohm}	Ohmic Resistance
j_{pot}	Current Density at a Fixed Potential
z	Electron Transfer Number
η	Overpotential
α	Charge Transfer Coefficient
F	Farraday Constant
R	Universal Gas Constant
T	Temperature
j_0	Exchange Current Density

Acknowledgement

I want to thank the DLR institute for networked energy systems in Oldenburg and especially Dr. Alexander Dyck and Mr. Peter Wagner for the opportunity to write my thesis and support me during it. Furthermore, I am thankful to Dr. Alexander Dyck for being the second supervisor to my thesis.

I wish to show my gratitude to Prof. Dr. Michael Wark for being the primary supervisor and the support from him and his working group in terms of scientific discussion and devise usage.

I would like to pay my special regards to my colleagues at the DLR institute and especially the fuel cell department. For all the advice during my research and tireless support. In particular, I want to thank Julia Hülstede for accompanying my thesis and constant advice, as well as constructive discussion.

I want to express my gratitude to the electron- and light microscopy service unit of the ultra-fast nanoscale dynamics working group of the university of Oldenburg for the opportunity for TEM measurements and in particular Dr. Erhardt Rhiel for the support during measurements.

Finally, I want to thank my friends and family for moral support during this work and during my whole university career. I am indebted to you for making it this far.

1 Motivation

The following decades are dominated by the impacts of climate change and the required technological challenges.[1] Emission of CO_2 is the main factor in terms of greenhouse gas contribution to climate alteration, therefore our energy system needs to be transformed, from a fossil fuel based one to renewable energies.[1,2] A cornerstone of this infrastructure at this point is energy storage and conversion. Hydrogen seems to be a suitable chemical storage solution, as it can be produced from carbon-based chemicals intermittently and electrochemically from water through electrolysis.[3,4] For energy conversion from hydrogen as a chemical storage to usable electrical and thermal energy, the fuel cell is an relatively efficient and emissionless prospect. It utilises the exothermic combustion reaction of hydrogen with oxygen to water and produces electricity and heat in the process.[4] The fuel cell can be used for many different sectors, such as off-grid energy production, decentralised urban electricity and heat supply or freight and passenger transportation.[4–7]

Especially in transportation, the proton-exchange membrane fuel cell (PEMFC) already finds commercialisation even though these systems are not yet mass-produced.[4–6] This technology is however still in its research and development phase and requires a lot of effort for large-scale and resource conserving implementation. Due to their excellent catalytic activity and adequate long-term stability carbon-supported platinum nanoparticles and alloys are used for both electrodes in current state-of-the-art PEMFC.[5,6] The cathode side poses the imminent research challenge, as the platinum loading is about 5-10 times higher, than on the anode, because of the considerably faster hydrogen oxidation reaction (HOR) on the anode in acidic media.[5,8] Extensive research has been conducted to improve mass-activity and lower the loading, as platinum is scarce in the earths crust and therefore expensive, even without current large-scale application of PEMFC in the automotive sector.[4,5] The price of a PEMFC stack is largely dictated by the platinum price, according to the USA Department of Energy, which is prognosed to increase even further with more demand in platinum.[9] The set cost threshold for consumer level fuel cell automotives of 20 US\$ $kW_{electric}^{-1}$ may be unreachable with platinum in both anode and cathode, due to the raw material price.[4] A similar performing non-platinum oxygen reduction reaction (ORR) catalyst could therefore accelerate the introduction of PEMFC in consumer systems. One of the currently most attractive replacements for

the cathode side catalyst are heat treated non-noble Me-N-C catalysts.[4,5,8] These catalysts are presumably comprised of carbon matrix embedded nitrogen functions, either occurring singular or in complexes with a metal ion.[5,10,11] A lot of research effort has already been put into these systems and produced catalysts with decent catalytic ORR activity, however lack long-term stability in acidic media and a high active site density, which in turn lowers their volumetric activity in comparison to platinum catalysts.[4,12,13] Different synthesis routes and precursors have been tested producing a wide variety of pathways for initially active catalysts, but stability investigations are scarce.[4,5,13,14] The most active metals turn out to be Fe and Co, each with up- and downsides in terms of their activity and physical and electrochemical properties. Bimetallic catalysts, especially with Fe and Co as metal species were investigated, due to a presumed synergistic effect between metals.[13,15] The combination of positive aspects of each metal could therefore lead to better catalysts, which circumvent flaws, like low stability and electrochemical selectivity. Binary Fe and Co Me-N-C catalysts were found to have average or better stability and activity than their monometallic counterparts.[13,16,17] In these studies however, bimetallic catalysts were only tested alongside the main focus on monometallic catalysts. The variation in metal contents was not further investigated and thus systemic effects omitted. A more systematic approach to different metal contents in bimetallic Me-N-C could lead to a better understanding of the structure-induced effects of each individual metal and electrochemical behaviour and is lacking in many studies to this day.

In this thesis mono- and bimetallic FeCo-N-C catalysts with a fixed metal content but different metal ratios are synthesised to investigate the influence of these different synthesis parameters. Spectroscopic, microscopic and diffraction techniques are used to elucidate catalysts properties and different structures based on metal ratio, which include transmission electron microscopy (TEM) with energy dispersive X-ray spectroscopy (EDS), X-ray photoelectron spectroscopy (XPS) and X-ray powder diffraction (XRD). The electrochemical properties of the catalysts are investigated in an rotating ring-disk electrode (RRDE) setup in acidic electrolyte with different techniques to determine electrochemical activity and selectivity. Cyclic voltammetry (CV) and electrochemical impedance spectroscopy (EIS) are utilised in conjunction with oxygen and nitrogen saturated electrolyte. Furthermore, an accelerated stress test (AST) is carried out, to determine the stability and AST-induced property changes of the produced catalysts.

2 Fundamentals

2.1 Proton Exchange Membrane Fuel Cells

The PEMFC is one promising approach to sustainable and renewable energy conversion, as it reacts hydrogen and oxygen from the air under controlled conditions to produce electrical energy, water and heat.[5,6,18] If the hydrogen is generated from a renewable source, such as water electrolysis in combination with solar energy, the process does not use fossil fuels and is environmentally sustainable. Besides the proton exchange membrane (PEM) variant of the fuel cells, various modifications exist for distinguished applications using different fuels and materials, like alkaline fuel cells or solid oxide fuel cells.[19–21] Even for PEMFC two variants exist, the high-temperature (HT) PEMFC, which operates at around 160 °C and the low-temperature (LT) PEMFC, below 100 °C.[22] The HT-PEMFC utilises a phosphoric acid soaked polybenzimidazole (PBI) membrane and is best suited for stationary and prolonged operation, due to the high operation temperature and subsequent longer start-up phases compared to LT-PEMFC.[18]

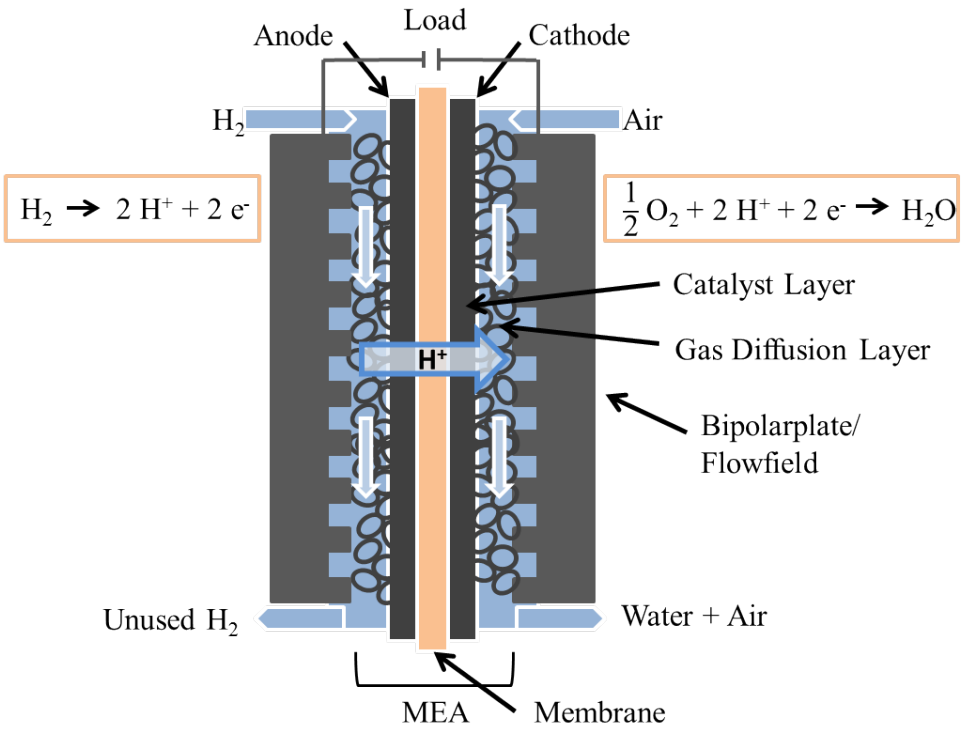

Figure 2.1: Schematic view of a single PEMFC with indicated parts and reactions.

With a lower operating temperature, the LT-PEMFC offers more flexibility and thus wider application in transportation and as transportable power sources.[6,18] Contrary to the HT-PEMFC, the LT-PEMFC employs a proton conducting sulfonated perfluoroethylene polymer membrane, called Nafion®. This membrane is sandwiched between the anode and cathode gas diffusion electrode, which are traditionally made of dispersed platinum nanoparticles on an electrically conductive, highly-porous carbon support (figure 2.1). Both catalyst layers are enclosed by gas diffusion layers (GDL), made from carbon fibers, to facilitate fuel transport in hierarchical pore systems. Membrane, catalyst layer and GDL together form the so-called membrane electrode assembly (MEA), which is encased by bipolar plates (BBP), made from metal or graphite, to provide electrical conductivity to the external circuit. These plates have the gas in- and outlets with flow patterns imprinted for gas distribution across the entire electrode surface. Hydrogen is fed on the anode side through the BPP and GDL to be oxidised on the electrocatalyst, generating a proton and electron.[6,18,22] The electron is conducted to an external load and becomes usable electricity, while the proton diffuses through the semi-permeable membrane to the cathode. Here, oxygen gets electrochemically reduced and combines with protons at the triple phase boundary between electrolyte, catalyst and gas phase to water, which gets exhausted.

2.2 Metal-Nitrogen-Carbon Electrocatalysts

The current and estimated rising cost of platinum metal used in catalysts hinders the large-scale introduction of PEMFC in the consumer sector.[4,5] Novel platinum-free catalysts are therefore imperative and research efforts have been on-going.[4,12,23] The harsh acidic and oxidising environment of the PEMFC poses a challenge to catalyst design as non-noble metal particles like iron, manganese or copper are too unstable in this regime to be considered as catalysts.[23] Therefore it is crucial to find alternative systems, that either do not incorporate metals or stabilise them sufficiently. Promising candidates are transition metal complexes with nitrogen and carbon, in which the metal ion is surrounded by nitrogen heteroaromatics comparable to pyridine and pyrrole derivatives.[4,12,23] These compounds derived from natural oxygen reducing enzymes, which occur unilaterally in organisms are called Heme/Cu terminal oxidases and have been known since the 1970s. The catalytically-active reducing sites in these enzymes are metal-nitrogen

macrocycles analogous to porphyrin and phtalocyanine (figure 2.2). Synthetically-made cobalt phtalocyanine catalysts by Jasinski et al. first showed ORR activity at room temperature in alkaline medium.[24] In the following years, it was demonstrated that different metal-nitrogen macrocycles were also active in acidic media.[12,25,26]

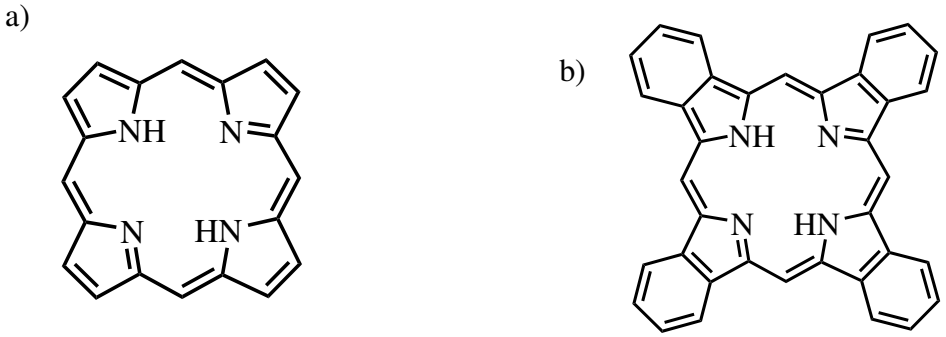

Figure 2.2: Chemical structures of a) porphyrin and b) phtalocyanine macrocycles.[23]

Additionally, Fe metal centers showed the highest activity with Co being second. Further studies by Jahnke et al. on unsupported and carbon-supported Me-N species showed, that a heat treatment under inert gas improves chemical stability and ORR activity.[27,28] It was believed that the heat treatment formed an active species of metal surrounded by doped nitrogen embedded in the carbon matrix, therefore making it less prone to chemical degradation. Yeager et al. later showed that the catalysts can be synthesised with separate metal salts and nitrogen-containing polymers on a carbon support, enabling different synthesis routes and corroborate the heat treatment as the vital part to active site formation.[29] This catalyst system has been intensively investigated over the years since and some different synthesis paths emerged. These combine early approaches of the heat treatment and individual precursors with modern catalyst design, like utilisation of metal-organic frameworks (MOF) and template methods.[5]

2.2.1 Synthesis Routes

A vast research effort has been put into Me-N-C electrocatalyst, presenting many different ways of production. Three different synthesis pathways can be identified, differing in precursors and catalyst design. Even though, different precursor materials and methods are used, the heat treatment step links all of these different paths together. During the heat treatment the precursor get transformed into a coherent catalyst and active sites are formed. Carbon atoms are converted to carbonaceous and graphitic structures during the heat treatment and nitrogen functions lead to pyridinic and pyrrolic moieties in the

carbon matrix. Depending on the temperature during the heat treatment different nitrogen containing functional groups are produced in different ratios. It was found, that a temperature between 800 and 1000 °C yields the most active catalysts, even though this is highly dependent on the exact choice of precursor materials.[5] The heat treatment can be performed under inert atmosphere like argon or nitrogen or in reactive atmospheres like ammonia, which can act as a nitrogen source during synthesis. In the following, three different synthesis methods are explained briefly, namely MOF, silica template and porous carbon support pathways.

Metal-Organic Framework

Just recently, MOFs were introduced in the field of Me-N-C catalysts, but shows promising future improvements as the MOF structure and tunability leads to a rational approach in design.[5,14] MOFs are comprised of a metal ion, most prominently Zn, surrounded by organic molecules acting as electron-donating ligands. These often build repeating units, resulting in a crystalline structure, which can incorporate a pore structure and subsequently high surface area.[5,14,30] For their use as Me-N-C catalysts MOFs are heat treated (figure 2.3), which leads to a conversion of the MOF to Me-N-C structures, which retain the order and pore structures of the initial MOF.[14,31] Herein, the active sites are uniformly dispersed, emphasizing the importance of high surface area. The properties of the resulting Me-N-C catalyst can be specifically tailored to the catalysts demands by choice of ligand and metal precursor in the MOF synthesis.[5] Catalysts made by this design, incorporating Co and Fe, showed high ORR activity in alkaline as well as in acidic media in RDE measurements.[14,32] Additional metals can be either introduced during MOF synthesis and directly build into the structure or exchanged later on in the pyrolysis step.

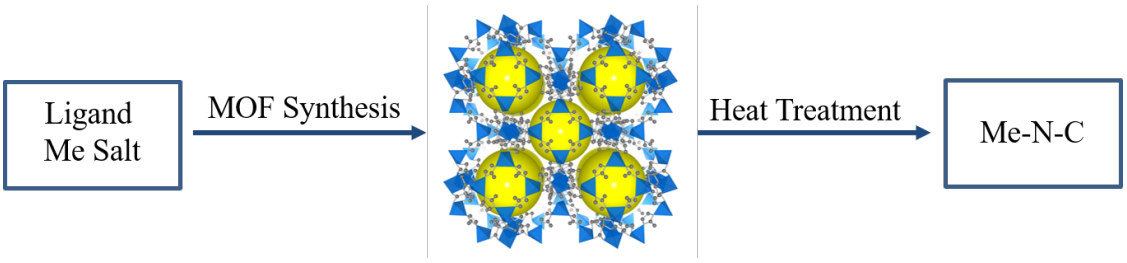

Figure 2.3: Overview of the Me-N-C synthesis using the MOF method. ZIF-8 image with permission from Fujie et al.[33] published by The Royal Society of Chemistry.

The metal substitution during the doping process proved to be useful with a lower second metal content, since pristine MOFs usually contain a high metal content, detrimental to the ORR activity of Me-N-C.[14] Even though MOF derived Me-N-C catalysts show excellent activity and durability, their cost as a precursor overshadows these and the synthesis is non-trivial, due to hazardous reagents such as hydroflouric acid.[12]

Silica Hard Template

The silica hard template approach to the synthesis of Me-N-C catalysts is akin to design in industrial heterogeneous catalysis with a hard template, on which the active components get deposited and the template later removed.[5] The as-made catalyst forms the negative of the template used. The catalysts properties can be controlled and tailored to the desired application for example porosity and surface area. A frequently used template is porous silica, like SBA-15, KIT-6 or MCM-41, as it can be easily made in different structures and removed by immersion in hydroflouric acid or concentrated potassium hydroxide.[5,34,35] This however presents a downside of this synthesis route as the handling of these chemicals requires certain protections and precautions. Precursors for the catalyst are available in a wide array of nitrogen-containing molecules, nitrogen polymers and monomers for *in-situ* polymerisation and metal salts.[5,34] This allows tuning of the catalyst, independent of the structural morphology provided by the template.[5]

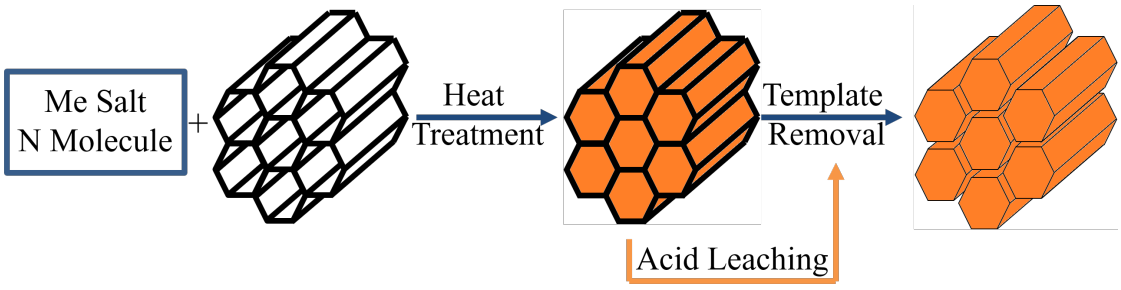

Figure 2.4: Overview of the Me-N-C synthesis path using silica hard templates with Me-N-C catalyst indicated in orange.

Porous Carbon Support

In contrast to the previously described synthesis methods of Me-N-C catalysts, the support based method allows a simple synthesis by combining a well-known carbon structure with a variety of N- and Me precursors.[5,12] Porous carbon supports have been extensively used for state-of-the-art platinum catalysts. They are readily available and

provide excellent properties in terms of electrical conductivity, surface area and pore morphology.[36,37] These can be brought together with a nitrogen source and metal moiety to form active catalysts during the heat treatment. Metal ions are often available through their simple salts, such as nitrates, acetates or sulfates, making them a cheap and available precursor. The nitrogen source offers even more variety as aminic, N-heteroaromatic, nitrogen polymers or nitrogen monomers for *in-situ* polymerisation can be used. The nitrogen source decomposes during the heat treatment and gets incorporated into defect sites of the carbon support matrix. Additionally, nitrogen precursors can form carbonaceous structures like graphene layers or carbon nanotubes on the support, which can vary widely depending on the specific precursor used.[12,38,39] These changes can also be pronounced in the electrochemical performance leading to different activities and peroxide yield as well as durability variances, depending on the nitrogen source.[12,40] During the heat treatment elemental metal particles or metal carbides can form from a surplus of available metal. Thus, acid leaching is carried out to dissolve metal particles but leave matrix incorporated active sites unaffected. Recently, multiple heat treatments have been performed in addition to acid leaching in order to remove remaining acid molecules and unstable carbon moieties.[16,41]

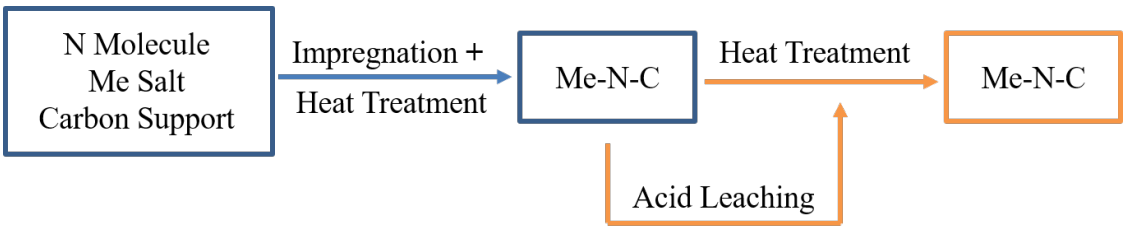

Figure 2.5: Flow chart of carbon support method for the Me-N-C synthesis with optional additional steps indicated in orange.

2.2.2 Active Site Discussion

The ORR mechanism in Me-N-C catalysts and the exact processes taking place on different groups in the catalyst remain elusive and a point of discussion. Molecular oxygen can be reduced to water in different mechanisms, utilising either 2 or 4 electrons.[10,12] The $2\,e^-$ pathway reduces O_2 only to H_2O_2, while the $4\,e^-$ mechanism avoids H_2O_2 formation and directly produces water. H_2O_2 is, due to its strong oxidation capabilities, detrimental to the fuel cell since it can oxidise the carbon support or degrade the membrane.[6,42] Peroxide formation is especially problematic with Fe or Co present in the catalyst, because these metals catalyse the Fenton reaction, forming reactive oxygen species from peroxides, which oxidise neighbouring carbon atoms rapidly, degrading the support.[42,43] The catalytically-active sites in Me-N-C catalysts remain a point of discussion, in-fact there are different sites contributing to ORR activity.[43] The postulated most active site is the metal complexed by four matrix incorporated pyridinic or pyrrolic groups and catalyses the $4\,e^-$ mechanism in the case of Fe and $2\,e^-$ mechanism with Co.[10,42,44]

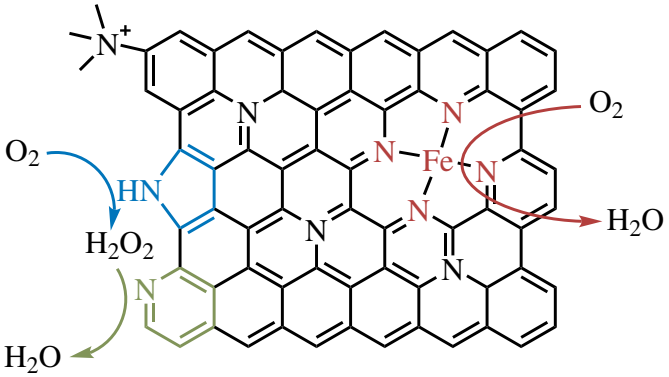

Figure 2.6: Schematic overview of different supposed active sites with indicated probable ORR mechanism.

Variations of these sites occur with differing numbers of complexing nitrogen groups and how these are incorporated in the carbon matrix. For example, in-plane sites (MeN_x) or at plane edges connecting adjacent carbon sheets (MeN_{2+2}), result in varying ORR activities and ORR mechanism selectivities.[10,44] Kramm et al. proposed the existence of active FeN_{2+2} sites preferably in micropores as connection of carbon sheets inside the pore, correlating the micropore volume of the support to ORR activity.[44] The determination of the exact nature of metal moieties in the catalyst is fairly difficult, since the

processes during heat treatment remain elusive and the characterisation of the catalyst is hindered by low metal content and sparse metallic sites.

Depending on the metal, spectroscopic techniques like Mössbauer, in the case of Fe, or X-ray absorption near edge structure (XANES) and extended X-ray absorption fine structure (EXAFS) can be employed, even though these are scarcely available.[17,44,45] Even without metals present, nitrogen doped carbon supports show ORR activity, although with a significantly lower activity in acidic electrolyte and selectivity than their metal-containing counterparts.[10,12,46] Pyridinic and pyrrolic groups in the carbon matrix show this activity towards ORR, with pyrrolic nitrogen presumably reducing oxygen to hydrogen peroxide in a $2\,e^-$ mechanism and pyridinic nitrogen further reducing the peroxide to water again with $2\,e^-$ resulting in $2 + 2\,e^-$ in total.[10] Nitrogen is also proposed to act as an n-type dopant, hence donates electrons to the carbon lattice, warranting further ORR activity.[47] A schematic overview of the different proposed active sites inside the carbon matrix can be seen in figure 2.6.

2.2.3 Bimetallic Catalysts

In the search for more active and durable Me-N-C catalysts different third period transition metals have been examined.[12,13,48,49] Using Fe as the metal component yields the highest ORR activity, with Co coming in second but lacking in terms of activity and selectivity. Co however shows higher durability than Fe catalysts in spite of the higher peroxide yield observed.[43,50]

One might assume that, the combination of positive properties of these metals might lead to more effective catalysts and has been investigated in different studies but just supplementary to monometallic catalysts. It led to contradictory results.[8,13] Martininaiou et al. found an ORR performance averaging that of Co and Fe monometallic Me-N-C catalysts when investigating bimetallic FeCo-N-C.[13] However, stability investigations on this catalyst led to a stronger degradation compared to the monometallic catalysts. Investigations from Wu et al. showed an increased stability in bimetallic FeCo-N-C, with the proposal of a stabilising influence of Co in the catalyst.[8] Interestingly, the bimetallic catalyst displayed a higher stability than monometallic Co-N-C suggesting synergistic effects through the incorporation of both metals. ORR performance-wise the bimetallic catalyst by Wu et al. lied in between both monometallic catalysts supporting the result by Martiniou et al.[8,13]

2.3 Electrochemical Characterisation

The electrochemical characterisation of novel electrocatalysts can be realised through testing in an rotating disk electrode (RDE) setup, which allows for facile and rather quick testing of new materials. This technique avoids non-trivial MEA manufacturing and requires much less material than catalyst testing in an actual fuel cell. RDE work in a three electrode setup with the catalyst applied in the tip of a rotating working electrode (WE).[51–53] In addition to the WE, a counter electrode (CE) and reference electrode (RE) are submerged in an electrolyte solution, providing electronic and ionic conductivity. The WE is comprised of an insulation mantle surrounding a disk electrode and can be seen schematically in figure 2.7.[51,54] The rotation of the WE leads to an outward laminar flow of electrolyte across the electrode surface induced by radial centrifugal forces, which can also be seen in figure 2.7.

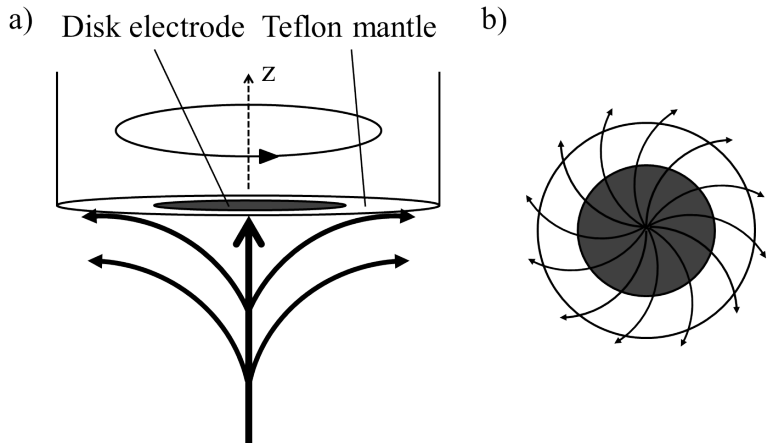

Figure 2.7: Schematic view of a RDE with indicated parts a) perpendicular to the rotation axis and b) along the rotation axis.

This leads to a constant flow of bulk electrolyte to the electrodes surface and thus an location independence of the measured current. The regime directly under the disk is the so-called diffusion layer, whose thickness is rotation speed dependent and mass-transport is only dictated by diffusion. Due to this arrangement the measured current underlies steady-state conditions, improving reproducibility and predictability of the system.[55] Thus at small overpotentials the current is only determined by reaction kinetics and charge transfer resistance with no mass-transport limitation. In figure 2.8 a schematic ORR curve can be seen with indicated parameters and mixed limited current area.

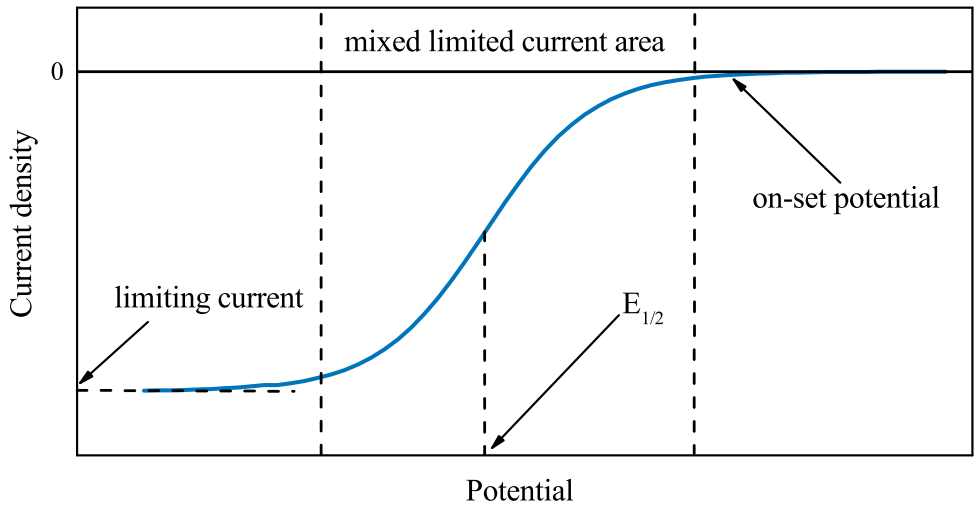

Figure 2.8: Schematic plot of an ORR curve with indicated limiting current, on-set potential and half-wave potential $E_{1/2}$.

With higher overpotentials the mass-transport becomes a limiting factor in the mixed limiting area.[51] At the boundary of these areas, the onset potential can be determined as an ORR performance indicator for the catalyst. In the mixed limited area the transition from kinetically to mass-transport limitation can be seen in the inflection point of the curve, which represents the half-wave potential. At high overpotentials the mass-transport becomes the limiting factor in the diffusion limited area. Since the mass-transport is dependent on the rotation speed of the WE, the limiting current density j_{lim} also varies with rotation speed. The reciprocal measured current densities j in the mixed limited area can be described as the sum of the reciprocal kinetic current density j_{kin} and limiting current density, as shown in equation 2.1.[12,55]

$$\frac{1}{j} = \frac{1}{j_{kin}} + \frac{1}{j_{lim}} \tag{2.1}$$

Thus the kinetic current density can be extracted by rearrangement of 2.1 to 2.2.

$$j_{kin} = \frac{j \cdot j_{lim}}{j_{lim} - j} \tag{2.2}$$

The kinetic current density can be used as a measure for the ORR performance of the catalyst in the form of the mass activity. Here, 2.2 is used with one j value at a certain potential, depending on the type of catalyst used, and related to the mass of catalyst applied to the electrode. Furthermore, the kinetic current density can be used to con-

struct a $\log(j_{kin})$ vs. E Tafel plot to determine the Tafel slope and exchange current for the reaction.[55] These parameters can give an indication to the rate-determining step of the electrochemical reaction and thus kinetic information. However, in the case of Me-N-C different active sites are present and thus multiple reactions occur, rendering a determination of the rate-determining step difficult.

A variant of the RDE is the addition of another electrode in the form of a ring around the disk electrode.[51,53–55] In this case the setup is called RRDE and the catalysts selectivity can be investigated to distinguish the 2- or 4- electron reaction pathways, related to the reduction to H_2O_2 or H_2O, respectively can be determined through the ring. A constant potential is applied to the ring, which oxidises or reduces side-products, which are thus detected and quantified.[51,53,56] The yield of side-product reacting at the ring is determined by the electrode geometry and a collection efficiency factor N can be measured, specific for each electrode. N can be determined through the ratio of the current density at the Ring j_R and the disk current density j_D according to equation 2.3.[51,53]

$$N = -\frac{j_R}{j_D} \tag{2.3}$$

In the application of ORR electrocatalyst testing, the H_2O_2 production during can be calculated using equation 2.4.[12,57]

$$X_{H_2O_2}(\%) = 100 \cdot \left(\frac{2j_R/N}{j_D + j_R/N} \right) \tag{2.4}$$

Here, X is the reaction yield, j_R is the current density measured at the ring electrode and j_D is the current density measured at the disk electrode.

2.4 Physical Characterisation

The following physical characterisation techniques, besides TEM, utilise X-rays to elucidate morphological and chemical properties. The physical processes and thus the gained information for each technique are presented in table 2.1. Each of them uses specific physical properties in order to provide information about the sample.

Table 2.1: X-ray characterisation techniques with their associated physical process and the information gained.

Technique	Process	Information
XPS	Emission of photoelectrons after X-ray excitation	Elemental and chemical surface composition
XRD	Diffraction of X-rays	Presence and structure of crystalline materials
EDS	Emission of X-rays after electron excitation	Elemental composition and spatial mapping

2.4.1 X-ray Photoelectron Spectroscopy

Principles

XPS is a destruction-free, surface-sensitive technique, used to investigate solid samples. Emission of an inner-shell electron from an element, due to the absorption of X-rays (figure 2.9) is utilised.[58]

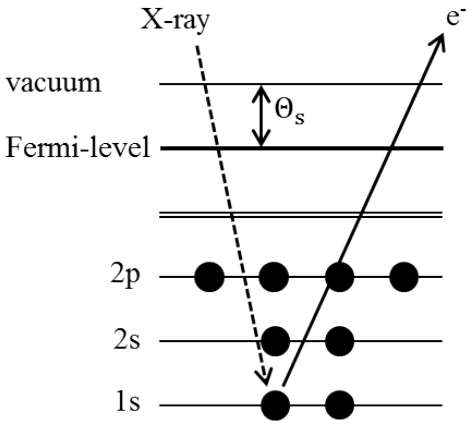

Figure 2.9: Schematic view of the primary emission process.

The emitted electrons carry a specific kinetic energy E_{kin}, which is the result of X-ray excitation energy $h\nu$, the work function of the spectrometer Θ_s and binding energy to its nucleus of the emitted electron E_B.[56,58] Rearranging this correlation for E_B yields formula 2.5. The electron E_B is according to Koopman's theorem, the difference of the electron energy in the atom compared to it's energy in vacuum.

$$E_B = h\nu - E_{kin} - \Theta_s \tag{2.5}$$

E_B is unique for each element and atomic orbital, which is useful for determination of the elements contained in a sample, their concentrations and chemical state. XPS analysis is surface-specific, because emitted electrons can only move a certain distance, before colliding with other electrons and subsequent loss of energy in inelastic collisions.[58,59] The mean free path $\lambda(E)$ of the electron is usually between four and eight atomic monolayers in the solid. Electrons, which emerge from deeper atomic layers are also detected, but at different binding energies, due to the energy loss in collisions. These electrons appear in the background of the spectrum and result in its usual step-like structure to higher E_B.

Secondary Processes and Doublet Splitting

The primary emission process can be followed by a secondary emission of an electron. These include the emission of Auger-electrons and X-ray fluorescence.[58] After the emission of a photoelectron the resulting electron hole can be filled by an electron from a higher atomic shell, emitting a second electron from the same or even higher shell, which is called an Auger-electron (figure 2.10.a). Kinetic energy of Auger-electrons is independent of the excitation energy, hence a shift in peak positions only occurs for photoelectrons after switching the X-ray wavelength. Secondary processes take place until the electron hole is propagated to the outermost atomic shells and is filled either through employed charge compensation or electrical connection of the sample holder. For XPS Auger-electrons are of secondary concern but constitute the investigative principal of Auger-electron spectroscopy (AES). Besides the emission of Auger-electrons, X-ray fluorescence can occur in competition with emitted X-ray irradiation instead of electrons, due to the same phenomena in the atom (figure 2.10.a). Additional to secondary emission processes, final state effects occur in XPS.

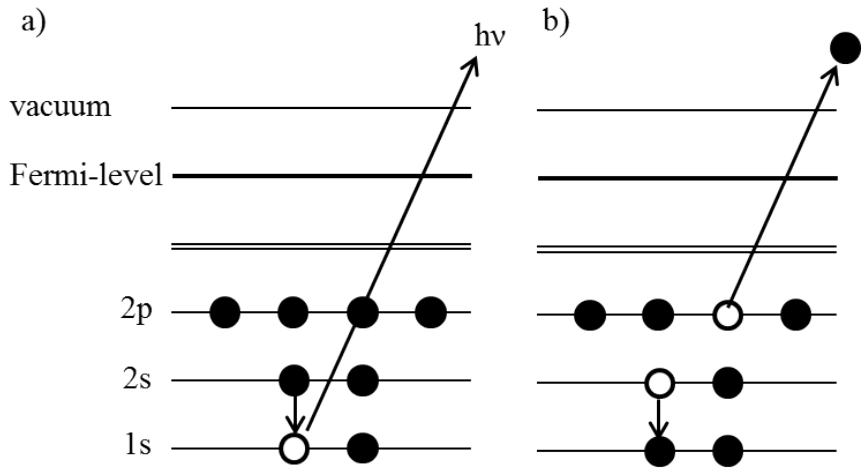

Figure 2.10: Schematic view of secondary emission processes: a) X-ray fluorescence, b) emission of Auger-electrons.

Spin-orbit splitting is one of these effects for emitted electrons from the p-, d- and f-orbitals. This effect leads to peak splitting with different relative intensities and stems from the interaction of the angular momentum and spin of the emitted electron. The sum of spin quantum number s and angular momentum number l is the total angular momentum quantum number J.[58,59] l adopts values according to the principal quantum number n as $l = n - 1$ and s is $\pm 1/2$. Therefore J adopts values depending on s and l as $J = |l \pm s| = 1/2, 3/2, 5/2$, etc. As a result of coupling between the spin and angular momentum, the binding energy is slightly shifted for different electrons from the same shell. Intensity ratio of the doublet peaks is dependent on the degeneracy $2J + 1$ of the specific orbital. The spin-orbit splitting is also element specific and can be utilised for qualitative analysis of the contained elements.

Further final-state effects are so-called satellites, which occur due to the change in effective nuclear charge after emission of an electron.[60] This change can excite electrons into higher shells, leading to a Shake-up effect. If the excited electron is emitted from the atom, the energy required to emit the second electron diminishes the kinetic energy of the primary photoelectron and results in a Shake-off effect. Normally these satellites occur in the spectrum with low intensity but can become significant in some transition metals, such as iron or cobalt.

Qualitative and Quantitative Analysis in XPS

A qualitative analysis about the surface's elemental content of a sample is possible, due to the element specific E_B. Signals can be attributed to certain elements with small E_B variations, due to different chemical states of the elements. At least two signals have to be identifiable and attributable to be able to unambiguously determine, whether an element is contained.[58,59] The variations in an elements E_B due to different chemical states is also called chemical shift, which is usually a few electronvolts. This shift is caused by inductive effects in the atom, in which electron density rises or falls around an atom, hence changing the binding energy to its electrons. Due to the chemical shift, one is able to make precise predictions about the specific chemical state of elements.
XP spectra can also yield data for quantitative analysis, in which a high resolution spectrum of an element is fitted utilizing algorithms in conjunction with literature results.[58,59] After removal of the spectrum background, the intensity I_i of the signal is described in a simplified approach by equation 2.6.[58]

$$I_i = L_i c_i \sigma_i K \lambda(E)_i \tag{2.6}$$

Here, L_i is the photon stream, c_i is the concentration of the element, σ_i is the photo ionization area or Scofield factor, K is an instrument specific constant and $\lambda(E)_i$ is the electron attenuation length. This so-called first principle approach omits sensitivity factors S, which are required by a highly detailed quantitative analysis. Assuming a constant X-ray stream and a homogeneous surface, atomic ratios can be determined using equation 2.7.

$$at.\%_i = \frac{I_i/S_i}{\sum I_i/S_i} \cdot 100\% \tag{2.7}$$

2.4.2 Transmission Electron Microscopy

With the TEM an electron beam can be utilised to observe the electron scattering behaviour of thin samples (< 1 µm) to image them.[61–63] Electrons are accelerated in an electric field and propagate through the sample, with almost no absorption processes.[63] While transmitting the sample, electrons get scattered by Coulomb interactions at atomic nuclei and electrons in an elastic and inelastic way, respectively.[61,63] When elastically scattered the electron loses only a very low amount of kinetic energy (< 0.2 %) in the

process. However, energy transferred to the nucleus could, with high-energy electrons, lead to displacement damage.[63] The scattering at electrons leads to a higher kinetic energy loss of the primary electron compared to the elastic scattering at nuclei. Transmitted electrons pass through the objective lens, while scattered electrons are blocked, resulting in a discrimination between scattered and unscattered electrons. For the detection of transmitted electrons, a phosphor screen is used, which emits photons under the impact of electrons.[63] Unscattered electrons, therefore appear white in the bright-field mode with highly scattering areas of the sample being darker. The scattering probability is also dependent on the atomic number, meaning heavier elements scatter more and appear darker in the resulting image. This also means, that the specimen thickness has to be lower for samples with heavier elements to achieve a sufficient transmittance and image quality.

Resolution of a TEM image is dependent on the kinetic energy of the electron beam, due to the wave-particle dualism resulting to a shorter wave-length with rising momentum.[61] The theoretical resolution of the TEM is given approximately by $\lambda/2$. Increasing the acceleration voltage a the resolution can shrink into pm regime, allowing for atomic scale microscopy.[63] Using high-resolution TEM (HR-TEM) it is possible to resolve the lattice structure of crystalline materials because of electron diffraction on nuclei analogous to traditional X-ray diffraction.

2.4.3 Energy Dispersive X-ray Spectroscopy

EDS is often used in conjunction with electron microscopy, as an electron beam is used for excitation.[61,63] The impact of electrons on inner-shell electrons leads to the excitation of said electron and subsequent relaxation under X-ray emission with an element specific wave-length.[62,63] This technique can therefore be used for elemental analysis on the sample. In the line scan method, the X-ray emission is recorded point by point and allows a spatial distinction of elements resulting in an elemental mapping throughout the sample.[62] One has to keep in mind, that peaks of different elements can overlap, due to the multitude of possible X-ray transitions, especially in heavier elements. As a result of reabsorption of emitted X-rays in the sample, photoelectrons, Auger-electrons or different X-rays can be emitted, which perturb the measurement and need to be accounted for.[61] Furthermore, Bremsstrahlung can be seen in the background of the spectra, which results from electrons passing by nuclei and slowing down, due to attractive Coulomb

forces, whereby X-rays are emitted.[62,63]

2.4.4 X-ray Diffraction

The structural investigation using XRD was proposed more than 100 years ago and remains a staple in crystallography.[56,64] It was discovered, that X-rays diffract on crystalline lattices, due to their wavelength being similar to atomic plane distances. The basis for modern XRD is Bragg's law, which states that two parallel incident beams on two lattice planes have two different path-lengths depending on the glancing angle θ (figure 2.11.a).[56,61,64] Interference occurs between the two beams, but is only constructively, if the path-length difference Δ is an integer multiple of their wavelengths. Therefore the lattice separation can be calculated using a glancing angle at which constructive interference occurs (equation 2.8).[56,64]

$$\lambda = 2d\sin(\theta) \tag{2.8}$$

Here, λ is the wavelength and d is the lattice separation. XRD can be used for non-destructive structure investigations of single crystals as well as crystalline powders. In powders, the crystalline domains occur in different orientations to each other.

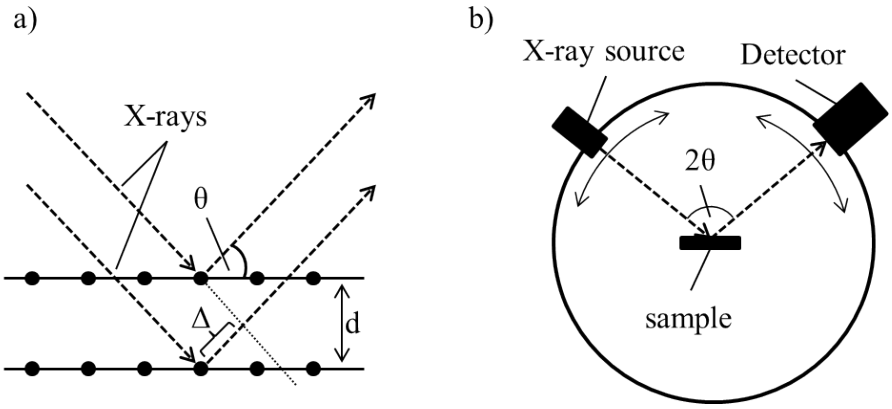

Figure 2.11: Schematic view of a) XRD on lattices with indicated lattice separation and glancing angle according to Bragg's law and b) Bragg-Bretano arrangement.

For powder investigations one possible arrangement is the Bragg-Bretano geometry, in which the X-ray source and detector are positioned around a flat sample and are rotated vertically to vary the glancing angle (figure 2.11.b.).[65] The sample can be rotated

around its axis to average the signal over differently oriented crystalline domains. In the analysis of Me-N-C catalysts this technique can be used to determine the presence of crystalline metal domains inside the powder using the Bragg-Bretano arrangement. Different chemical constitution of these metals can be identified, such as oxides or metallic phases.[65]

3 Experimental Procedures

3.1 Synthesis of Mono- and Bimetallic Fe/Co-N-C Electrocatalysts

Preceding catalyst synthesis the carbon support material was oxidised according to the procedure from Schmies et al.[46] As carbon support a carbon black *Black Pearls 2000* (2.0 g, Cabot, Boston, MA, United States of America) was dispersed in concentrated HNO_3 (200 mL, 65%, Carl Roth, Karlsruhe, Germany) in a round botton flask with attached reflux condenser and held at 90 °C for 5 h. The product was subsequently washed with water (Milli-Q, 18.5 MΩ cm^{-1}) until neutral pH and dried under reduced pressure at 30 °C overnight.

The catalyst synthesis was adapted from Chung et al. and optimised in previous PhD work in terms of experimental conditions and weight ratios.[40] The oxidised Black Pearls (BP_{ox}, 105.0 mg, 19 wt.%) were impregnated with cyanamide (443.0 mg, 80 wt.%, Sigma-Aldrich, St. Louis, MO, United States of America) and metal salts iron acetate $FeAc_2$ (Sigma-Aldrich) and/or cobalt acetate $CoAc_2$ (Sigma-Aldrich) dissolved in ethanol (4.0 ml, Fisher Scientific, Pittsburgh, PA, United States of America). The metal weight ratios were varied according to table 3.1 to a total of 1 wt.% (0.1 mmol) metal ion. The mixture was kept in an ultrasonic bath until complete evaporation of the ethanol and afterwards dried under reduced pressure at 30 °C overnight. The impregnated carbon support was ground in a mortar to a fine powder, followed by a first heat treatment in an *RHTC 80-230/15* tube furnace (Nabertherm, Lilienthal, Germany). The heat treatment consisted of heating to 900 °C with 5.0 °C min^{-1} under N_2-atmosphere and holding for 1 h with subsequent cooling to room temperature. Afterwards, the product was added to 2 M H_2SO_4 (30.0 ml, Carl Roth) in a round bottom flask with attached reflux condenser and held at 90 °C for 16 h. The acid was removed by filtration and multiple washes with ultrapure water until pH-neutral and then dried under reduced pressure at 30 °C overnight. Finally, a second heat treatment in the tube furnace was carried out analogous to the first.

Table 3.1: Metal ion ratios indicated in wt.% of the total synthesis weight.

Synthesis	Fe-N-C	FeCo-N-C (3:1)	FeCo-N-C (5:3)
Fe^{2+}	1	0.75	0.63
Co^{2+}	0	0.25	0.37
Synthesis	FeCo-N-C (1:1)	FeCo-N-C (1:3)	Co-N-C
Fe^{2+}	0.5	0.25	0
Co^{2+}	0.5	0.75	1

3.2 Electrochemical Characterisation with RRDE

3.2.1 Electrochemical Setup

Prior to usage the electrochemical glass setup including the cell was thoroughly cleaned by submerging in concentrated H_2SO_4 mixed with a small amount of H_2O_2 producing so-called piranha solution. After 24 h the glasware was rinsed multiple times with ultrapure water and stored in it until utilisation. A reversible hydrogen electrode (RHE) was used in the setup and calibrated before use. Calibration was carried out in a three-electrode setup with a platinum disk working electrode and platinum wire counter electrode in 0.1 M $HClO_4$ electrolyte (Merck, Darmstadt, Germany). The Pt-working electrode was electrochemically cleaned with CV according to the protocol in table 3.2 without rotation of the electrode in nitrogen saturated electrolyte. Afterwards, the RHE was calibrated at 1600 rpm starting with an open circuit potential (OCP) measurement in hydrogen saturated electrolyte.

Table 3.2: RHE reference electrode calibration protocol.

Technique	Scans	Potential Range vs. RHE [V]	Scan Rate [mV/s]
CV	3	0.05 – 1.2	20
CV	200	0.05 – 1.2	500
CV	3	0.05 – 1.2	20
		OCP measurement (15 min)	
CV	5	OCP $\pm$ 0.005	1

The *AFE7R9GCPT* RRDE working electrodes (Pine Research Instrumentation, Durham, NC, United States of America) used for catalyst characterisation consisted of a 0.2475 cm^2 glassy carbon disk and 37 % collection efficiency platinum ring embedded in a polytetrafluoroethylene (PTFE) shroud. The used setup is displayed in figure 3.1. Prior to catalyst coating, the electrodes were polished to ensure an even and clean surface. Polishing was carried out with 1.0 µm and 0.05 µm aluminium oxide abrasion suspension *MicroPolish 40-10081* (BUEHLER, Lake Bluff, IL, United States of America) sequentially for 5 min each. Afterwards, the electrodes were ultrasonicated, first in isopropanol (Fisher Scientific) and then in ultrapure water for 10 min each.

The catalyst ink was prepared by ultrasonicating catalyst powder (3.0 mg), ultrapure water (280.8 µL) and isopropanol (63.0 µL) for 15 min and subsequent addition of Nafion (5.0 wt.%, 38.1 µL, Sigma-Aldrich) and for ultrasonication for 30 min. As prepared ink (12.4 µL) was deposited on to the cleaned glassy carbon disk, briefly pre-dried at 60 °C for 5 min and completely dried at room temperature in ambient air. Afterwards, the electrodes were covered with a droplet of water to store over-night.

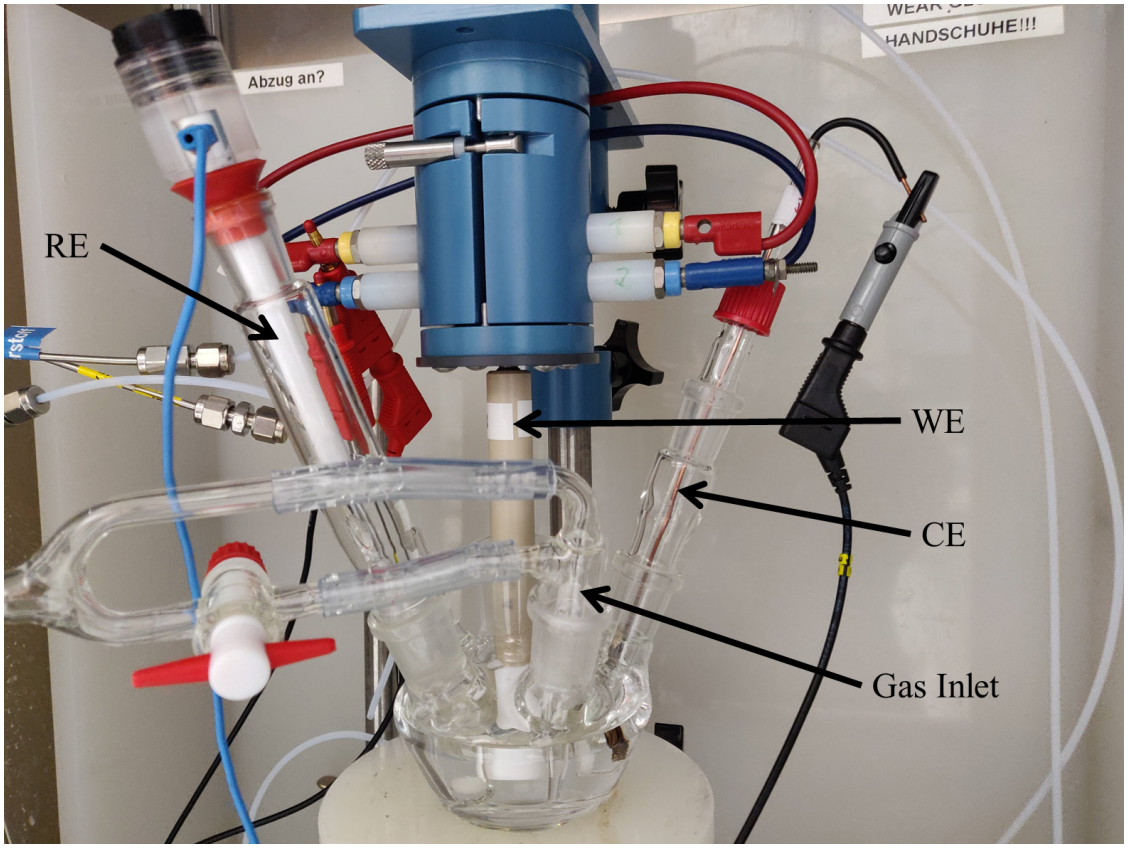

Figure 3.1: Photograph of the electrochemical setup used.

3.2.2 Measurement Techniques

All electrochemical measurements were carried out in 0.1 M $HClO_4$, which was saturated with either oxygen or nitrogen gas for 15 min prior. During measurements the respective gas was flowing over the electrolyte surface. For potentiostatic control a *PGSTAT128N* (Metrohm Autolab, Utrecht, Netherlands) was used and handled by *Nova 2.1* (Metrohm Autolab) software.

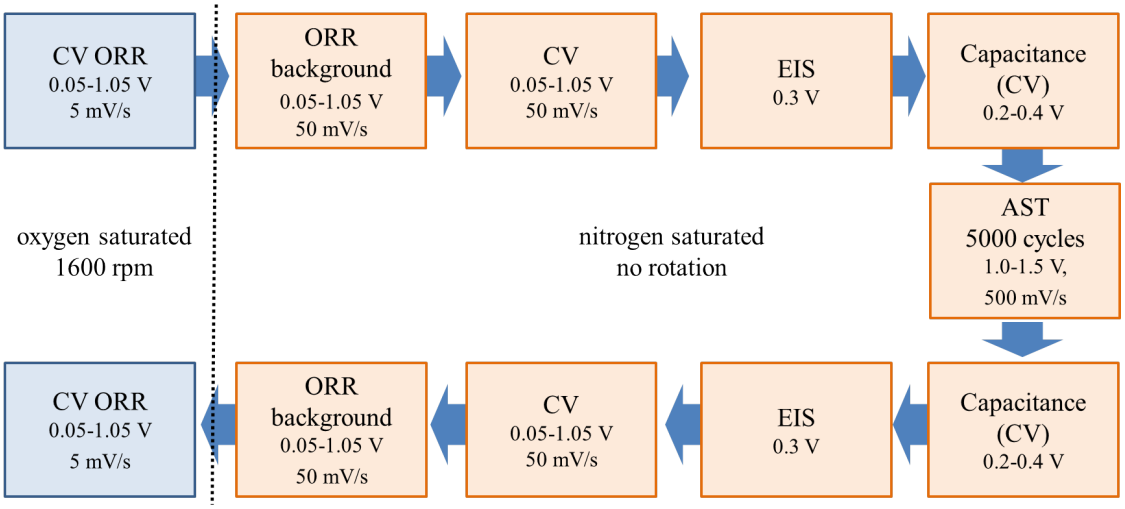

Figure 3.2: Flow sheet of the electrochemical characterisation procedure including potential ranges and scan rates, as well as indicated rotation speed and electrolyte gas saturation: oxygen (blue), nitrogen (orange).[13]

The electrochemical characterisation of catalysts was adapted from Martinaiou et al.[13] and carried out according to figure 3.2, namely initial characterisation, an accelerated stress test to induce degradation and another characterisation to evaluate the changes in performance. CVs were recorded in oxygen saturated electrolyte and a rotation rate of 1600 rpm. Three CV scans were recorded between 0.05 and 1.05 V with a scan rate of 50 mV s^{-1} and the last two scans were averaged for evaluation. The ring electrode was held at a potential of 1.2 V vs. RHE. Further measurements of the initial characterisation were carried out in nitrogen saturated electrolyte without electrode rotation. In order to correct the ORR curves for capacitive currents, the same ORR protocol was carried out again without oxygen present in the electrolyte. Afterwards, three CV scans were carried out between 0.05 and 1.05 V with a scan rate of 50 mV s^{-1}. Internal resistance (iR) correction, mainly attributed to ionic resistance in the electrolyte, was achieved through measurement of EIS at 0.3 V with an amplitude of 10 mV and a frequency range from 100 kHz to 0.1 Hz.[66,67] Finally, a capacitance analysis was done with CVs at different

scan rates between 0.02 and 0.16 V s^{-1} in 0.02 V s^{-1} steps, in a potential window from 0.2 to 0.4 V. Stability of the catalyst was investigated by an accelerated stress test in a potential range from 1.0 to 1.5 V and a scan rate of 500 mV s^{-1} for 5000 cycles.[13,68] After the stress test, analogous characterisations to initial measurements were performed with the ORR curve last, to avoid switching gas saturation multiple times over.

3.2.3 Data Evaluation of Electrochemical Measurements

Electrochemical data of the examined catalysts were analysed and parameters calculated with custom-made analysis software, coded in Python 3. Background correction of the ORR curve was achieved through subtraction of the ORR data recorded under oxygen with the data under nitrogen, since potential ranges and scan rates are identical. For iR-drop correction, the ohmic resistance was extracted from impedance spectra at the zero point of the real part Z'' of the impedance and the corrected potential calculated according to equation 3.1.[67]

$$U_{corr} = I \cdot R_{Ohm} \tag{3.1}$$

The onset potential of the ORR curve was extracted by normalising the data and returning the first point that reaches 2 % of the maximum current density. Moreover, the maximum value of the first derivative of polarisation data yielded the halfwave potential as this is the inflection point of the curve. Electrochemical mass activity is defined as kinetic current density j_{kin} in regard to catalyst mass and can be calculated with the limiting current density j_{lim} as the maximum negative current density value and current density at a fixed potential j_{pot}, in this thesis 0.75 V. Peroxide yield $X_{H_2O_2}$ and electron transfer number z required the ring current recorded in RRDE experiments as well as the disk current. For both, the average ring and disk current density between 0.1 and 0.7 V was determined and inserted in equations 3.2 and 2.4.

$$z = \frac{4 j_D}{j_D + j_R/N} \tag{3.2}$$

Tafel analysis was performed according to the rearranged Tafel equation 3.3 for low overpotentials with the corresponding Tafel plot of $\log(j_{kin})$ versus η. An exemplary Tafel plot is shown in Figure 3.3, in which the linear area in the low overpotential region of the curve is extrapolated and the slope and y-intercept calculated. The slope is in the form of $-(1-\alpha)zF/2.3RT$ for reduction reactions, where α can be calculated by

inserting the constants R, F and the known temperature T. The y-intercept in this plot is $\log(j_0)$, which can be extracted through exponentiation to base 10.

$$\log(j_{kin}) = \log(j_0) - \frac{(1-\alpha)zF}{2.3RT} \cdot \eta \tag{3.3}$$

Here, j_0 is the exchange current density, α is the dimensionless charge transfer coefficient, R is the universal gas constant, T is the temperature and η is the activation overpotential.

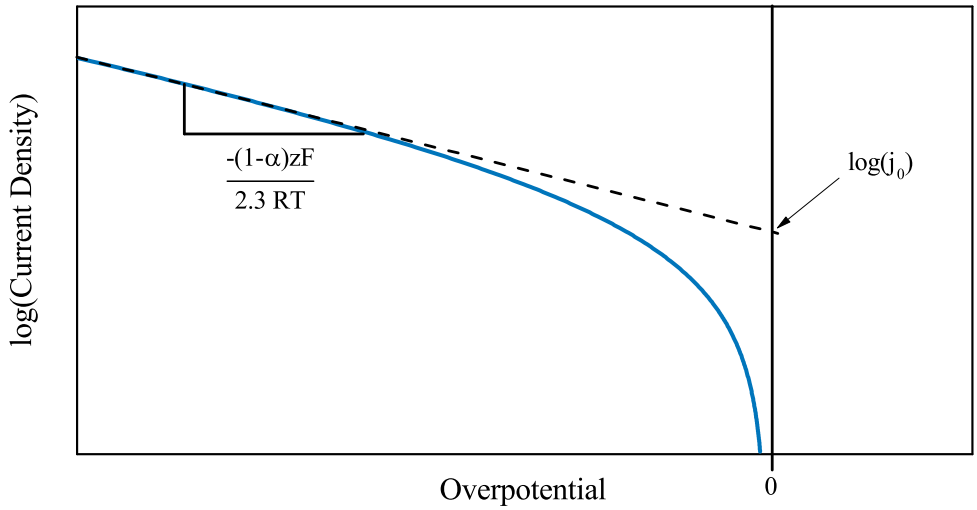

Figure 3.3: Schematic Tafel plot of a reduction reaction with indicated slope and y-intercept.

3.3 Microscopy

TEM

For TEM measurements, catalyst powder (2.0 mg) was dispersed in isopropanol (3.0 mL) and briefly ultrasonicated. The resulting suspension was dropped (3.0 µL) on *Polioform* (polyvinyl butyral)-coated copper meshes (Plano GmbH, Wetzlar, Germany) and dried in ambient air. To check whether the polymer film was damaged and if sufficiently thin particles are present, the samples were reviewed with a *EM902A* TEM (Zeiss, Oberkochen, Germany) at Universität Oldenburg with 80 kV acceleration voltage. Afterwards the samples were introduced to the HR-TEM a *JEM-2100F* (Jeol, Akishima, Japan). This device operates with a ZrO/W(100) Schottky field emission electron source and accel-

erating voltages of 80 – 200 kV. The measurements were conducted in the electron microscopy facility of the Carl-von-Ossietzky University of Oldenburg with Dr. Erhard Rhiel.

3.4 Spectroscopy

XPS

XPS measurements were carried out using an *ESCALAB 250Xi* (Thermo Scientific Fisher, Waltham, MA, United States of America) at the Carl-von-Ossietzky University of Oldenburg in conjunction with the *Avantage* software (Thermo Scientific Fisher). X-rays have been produced with a 1486.6 eV aluminium K_α source and subsequentially monochromated with a ray diameter of 500 μm. The samples were compacted in an aluminium sample holder to avoid contamination of the device. Samples were hold in a preparation chamber until the pressure reached 10^{-8}–10^{-7} mbar and then brought in the analysis chamber. Measurements were performed at a pressure lower than 10^{-9} mbar and a charge compensation was introduced using an electron flood gun. This was necessary, due to electrical charges building up in the sample during the emission of electrons. For each sample a survey spectrum and high resolution spectra of elements of interest were recorded until no change in values occurred any more. The measurement parameter are listed in table 3.3. High resolution spectra were recorded for C1s, O1s, N1s, Fe2p and Co2p. Quantitative analysis of the high resolution spectra was performed using the Avantage software, in which the background and peaks were fitted according to literature parameters.

Table 3.3: XPS measurement parameters for survey and high resolution spectra.

parameter	Survey	High-Resolution
Pass Energy [eV]	10.0	20.0
Dwell Time [ms]	50	50
Step Size [eV]	1	0.02

EDS

EDS was used in conjunction with HR-TEM using a *Oxford INCA TEM250* with *X-Max80 SDD*-detector (Oxford Instruments, Abingdon, United Kingdom) of 80 mm^2 area. Particles were previously identified in TEM mode and then measured through an elemental mapping over the particles. Data analysis and visualisation was done in *INCA* analysis software (Oxford Instruments).

3.5 Diffraction

XRD

For XRD sample preparation, about 10 mg of sample was dispersed in 100 µL isopropanol under short ultrasonication. 60 µL of the resulting ink was spread on an amorphous silicon disk and dried in air until the alcohol evaporated. Afterwards, samples were introduced into an *EMPYREAN* X-ray diffractometer (PANalytical, Kassel, Germany) with an Bragg-Bretano powder diffraction arrangement and irradiated with K_α X-rays from an copper-anode under 40 kV and 40 mA. Diffractograms were recorded in 5–90 ° 2θ region with Julia Hülstede at Universität Oldenburg and data was analysed using *HighScore Plus* software (PANalytical).

Figure 3.4: Photograph of the *EMPYREAN* X-ray diffractometer.

4 Results and Discussion

Hereinafter, observations and experimental data will be evaluated and discussed. First, observations during the synthesis of the catalysts will be examined, followed by an in-depth analysis of the morphology and chemical composition. Afterwards, the electrochemical data will be evaluated and differences in electrochemical and behaviour compared. Finally, the morphology and chemical composition will be associated with the electrochemical properties and possible synergistic effects of the metal ratio assessed.

4.1 Catalyst Weight Changes During Synthesis

For a systematic investigation of the influence of the Fe/Co ratio on the physical and electrochemical properties of Me-N-C catalysts, five different Me-N-C catalysts with differing Fe/Co ratios were synthesised according to the same synthesis route and experimental conditions. The metal ratios differed each by 0.25 wt.%, providing a reasonable resolution of differing catalyst properties. In the analysis of the electrochemical characterisation, discussed in later sections, property differences became apparent, demanding another catalyst between 0.75 and 0.5 wt.% Fe. Therefore, a 0.63 wt.% Fe catalyst was synthesised, resulting in a total of six Me-N-C catalysts to be compared.
During the synthesis, no differences between the appearance of samples were observed. Only a slightly lower dispersibility in ethanol or isopropanol with rising Co content in the final catalyst was observed. The weight change of the samples during synthesis can give indications to processes during the heat treatment and acid washing steps. Figure 4.1 shows the percentage weight loss of the sample with each synthesis step. During the first pyrolysis, the sample weight decreased by about 80 wt.%. Tian et al. proposed the first heat treatment decomposes most of the cyanamide, doping the carbon matrix with the released nitrogen and forming ORR active species.[69] Thus most of the mass of the cyanamide will be gone from the sample. In-fact, the amount of weight change during the first heat treatment correlates with 80 wt.% cyanamide used in the synthesis. Besides the decomposition of cyanamide and incorporation of nitrogen into the carbon matrix, oxygen functionalities in the carbon support get decomposed and released as CO and CO_2 but to a lesser extent compared to the cyanamide, only about 5 wt.% according to Tian et al.[69] The weight change during the subsequent acid leaching step varies

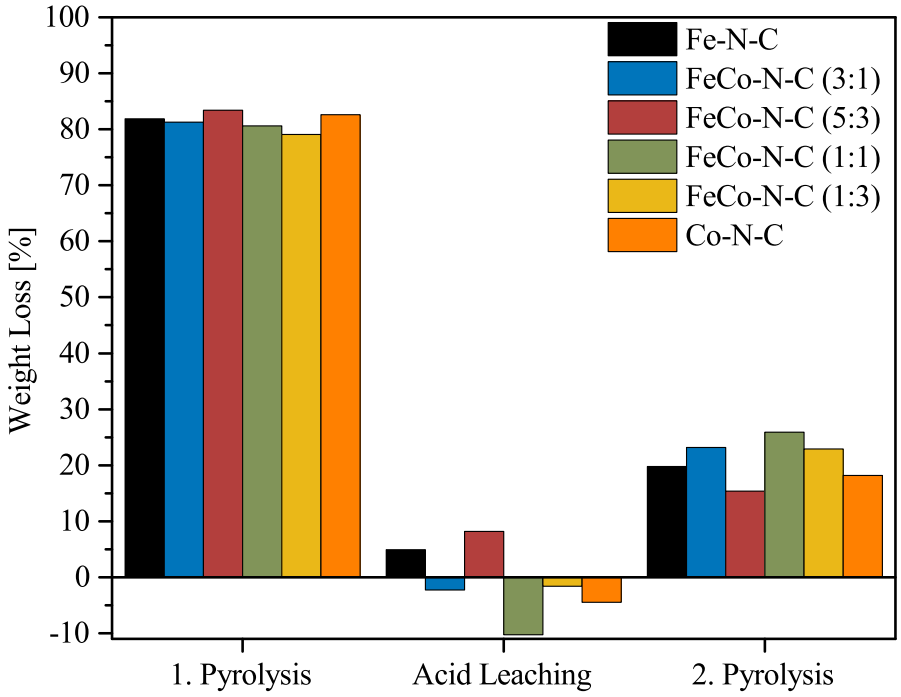

Figure 4.1: Subsequent weight loss percentage after each synthesis step.

across all samples between a loss of 10 wt.% and a gain up to 10 wt.%, compared to the once heat treated catalyst. The acid leaching removes metal particles but can also adsorb species on the catalyst and thus may explain the weight changes, due to different amounts of additional species adsorbing and formed particles being removed.[69] It was also reported that metal particles can be enveloped in a carbon shell, rendering them resistant to acid dissolution; therefore, contributing to an uneven weight loss between samples, as different amounts of these shell-core like structures may be formed.[16] After the second pyrolysis, all samples lost weight in differing amounts, but the overall weight loss of acid leaching and second pyrolysis remains similar across all samples at around 15–20 wt.%. This suggests, the weight increase after the acid leaching is due to adsorbed species, for example sulfates, which get removed during the second heat treatment along with residual cyanamide and strongly oxidised carbon in the support.[69] Sample losses could also be introduced during experimental work up in the filtration of catalyst-acid dispersion and subsequent drying. Ultimately, there seems to be no causality between the weight loss during synthesis steps and metal ratio, as all samples experience about the same weight decreases stemming from a plethora of fluctuations during harsh synthesis conditions and experimental challenges.

4.2 Physical Characterisation of Mono- and Bimetallic Me-N-C

The six synthesised catalysts will be characterised and evaluated regarding their morphology, surface elemental and functional group composition. Additionally, the presence of undesirable metal particles will be assessed.

The crystalline domains of the unwanted particles can be detected by XRD. Diffractograms for all synthesised catalysts and the oxidised Black Pearls support are shown in figure 4.2. In all catalyst samples, amorphous peaks are visible at 2θ values of 25 °, 43 ° and 83 °, which are also present in the neat Black Pearls reference material. At a 2θ value of 26 °, another peak, though fairly small, may be present. It is visible for FeCo-N-C (3:1), FeCo-N-C (5:3) and FeCo-N-C (1:3) but is barely recognisable in the other catalysts. This peak may be attributed to graphitic carbon as reported by Li et al.[70] and Carmo et al.[71] in similar carbon materials.[15]

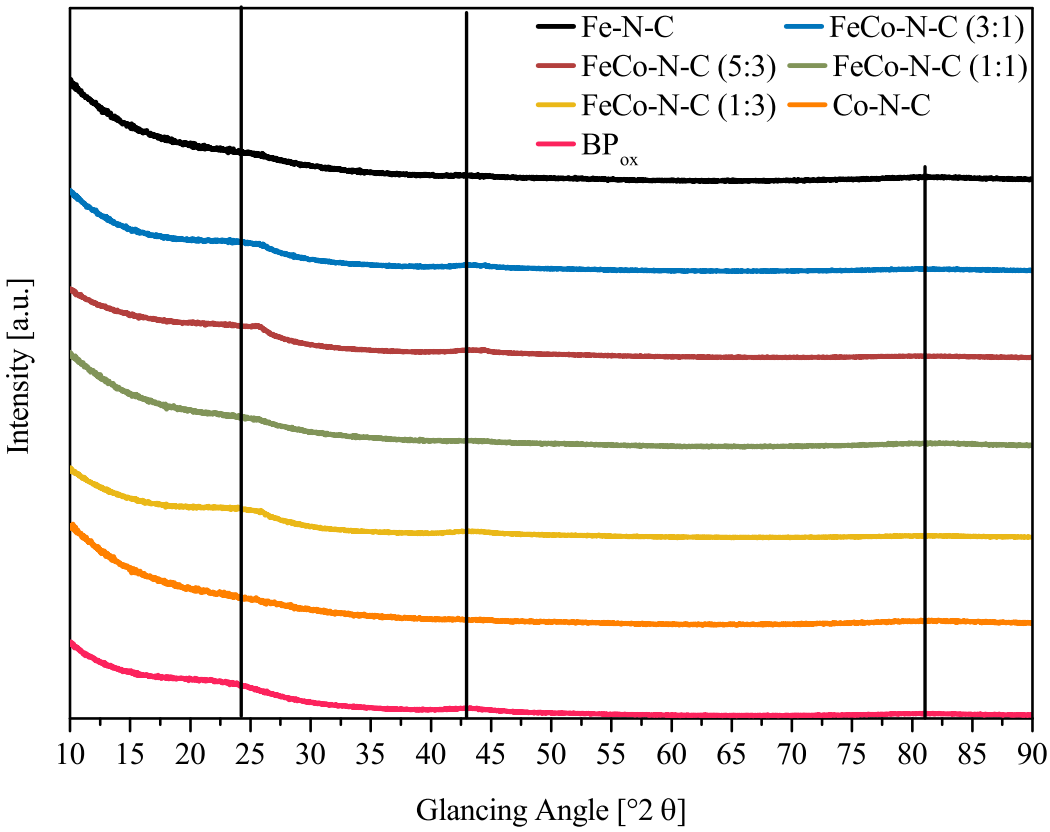

Figure 4.2: XRD of synthesised catalysts with indicated Black Pearls reference peaks.

Alternatively, MeC_3 could cause a peak at this glancing angle but further peaks, which would be at a 2θ value of 43 °, are not distinguishable from the reference peak at this angle.[72–74] Overall the diffractogram is as expected for Me-N-C catalysts and no strong indication of a high metal particle presence can be seen.[13]

Morphological studies, using HR-TEM with EDS, were carried out to asses the structure of carbon particles and their elemental composition. Representative for all bimetallic catalysts, a HR-TEM micrograph and its EDS mapping of FeCo-N-C (5:3) are presented in figure 4.3 and all remaining micrographs and EDS mappings in appendix figure 7.3.

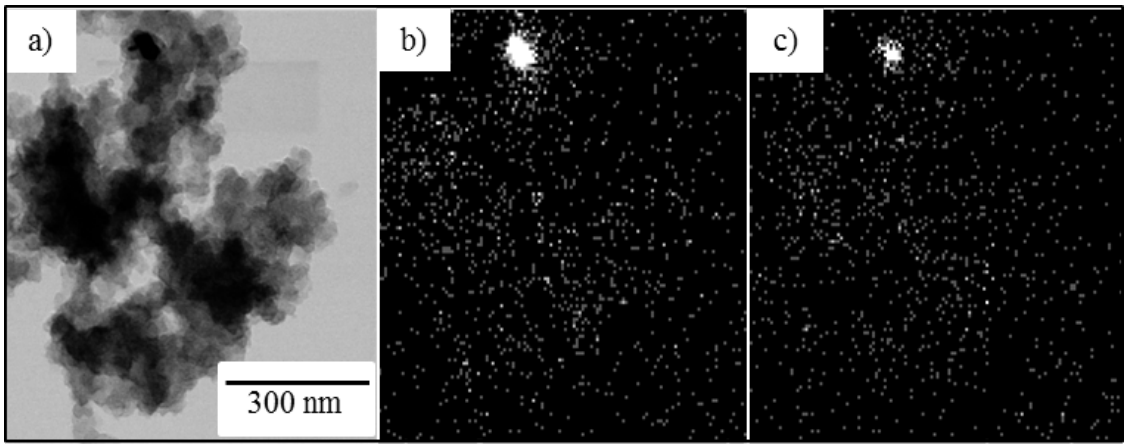

Figure 4.3: a) HR-TEM, b) Fe EDS mapping and c) Co EDS mapping micrographs of the FeCo-N-C (5:3) catalyst.

White spots are visible in spots where no carbon particle is present, which stem from background X-ray radiation such as Bremsstrahlung. However, an atomic distribution of metal correlating with the carbon particle can be seen for Fe and Co as individual white dots in the EDS mapping. As reported by Chung et al., this can indicate a distribution of $Me-N_x$ sites across the whole carbon structure and thus facilitates ORR activity.[11] However, an agglomeration of both elements is visible, hinting at metal particles. Interestingly, Fe and Co agglomerate in the same locations, coinciding with deep dark spots in the TEM micrograph. These agglomerations occur in all catalyst samples with no clear indication of differing populations depending on metal ratios. No presence of metal particles could be observed in XRD, as seen previously, which indicates a fairly low amount of particles. The amount is still fairly small compared to other catalysts in the literature with similar synthesis strategies.[17,75] The heat treatment of Me-N-C catalysts may lead to the formation of metal particles.[13,73] It seems the creation of particles is not fully avoidable but also pose no significant drawback as long as the amount remains minimal.

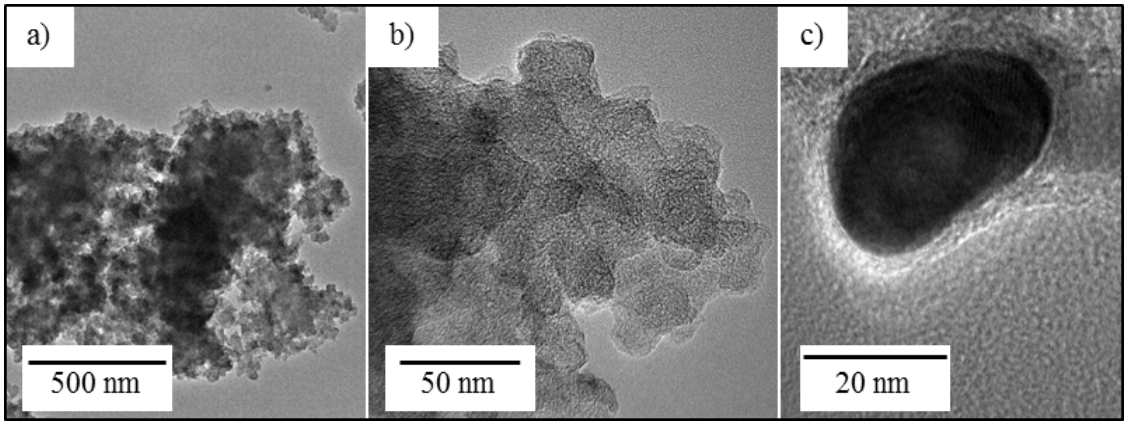

Figure 4.4: HR-TEM micrographs of a) FeCo-N-C (5:3), b) FeCo-N-C (5:3) and c) metal particle enveloped by carbon in FeCo-N-C (3:1).

A HR-TEM micrograph of a particle can be seen in figure 4.4b. The metal particles are apparently resistant to dissolution during the acid leaching step in the synthesis. It was reported that these metal particles are enveloped by a carbon shell preserving them.[16,49] The darker part represents the metal in comparison to the lighter carbon surrounding it. A few nanometer thick shell of carbon is visible on the lower side of the particle with visible layers corresponding to the graphitic morphology. Carbon enveloped metal particles may be more resistant to dissolution but long-term stability is not guaranteed as carbon corrosion can open the carbon shell and expose the metal particle to the acidic media. Furthermore, metal particles in the form of carbides may also be ORR active.[15,43,72] Consequently, the stability of Me-N-C catalysts with metal particles present may be relatively lower, due to the dissolution of active carbide species in long-term application.
The carbon support shows a morphology typical of the Black Pearls carbon black used during synthesis (figure 4.4b).[71] It consists of electronically conducting turbostratic carbon layers, resembling pearls, in a densely packed network. The structure of the carbon support seems to be uniform across all synthesised catalysts, undergoing overall the same processes during the synthesis.
XPS gives an indication of the chemical nature of the elements in the catalyst's surface. It can give a hint to the chemical composition of the metal species as to whether they occur ionic or as metal particles. As depicted in figure 4.5, the Fe2p signal has a fairly high signal-to-noise ratio, limiting an in-depth analysis and spectrum fitting. Nonetheless, it seems evident that the Fe signal appears only at E_B values over 710 eV and Co signal over 778 eV suggesting an oxidised state, thus precluding elemental Fe presence.[15]

Additionally, elemental Fe and Co XRD peaks do not coincide with observed peaks and thus are not visible in the diffractogram.[17,76,77]

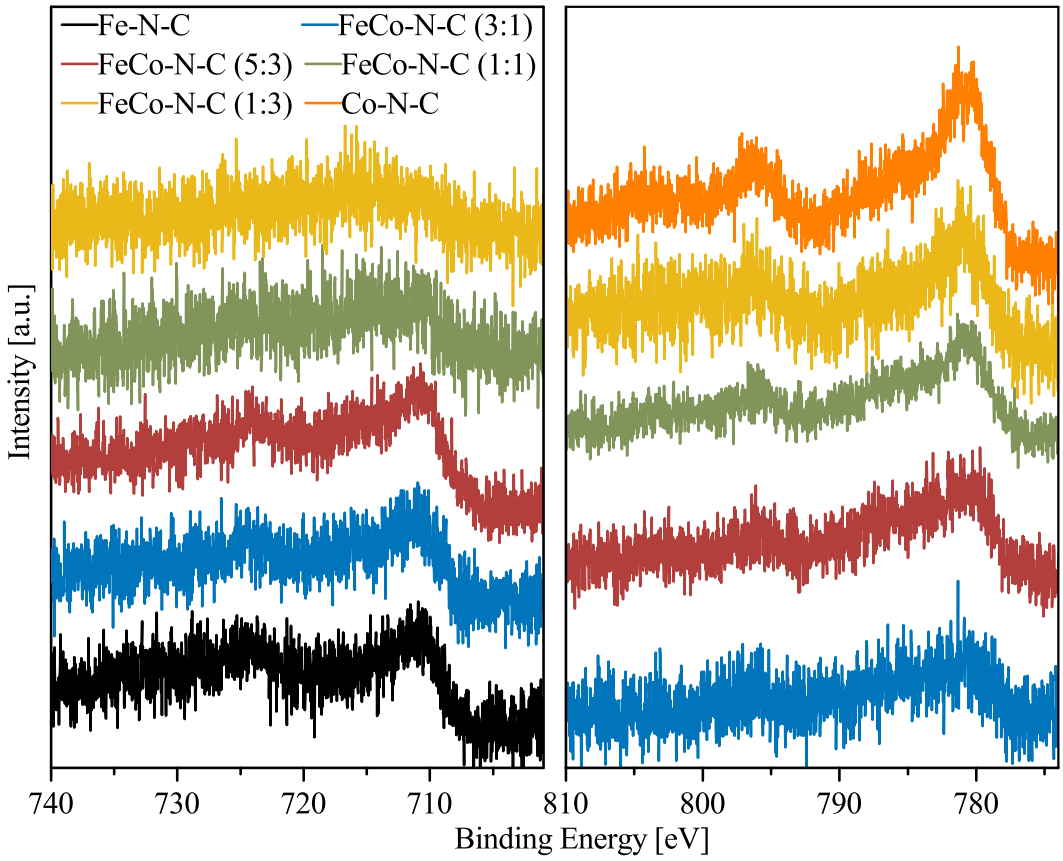

Figure 4.5: Fe2p (left) and Co2p (right) high resolution XP spectra of all Me-N-C catalysts.

The elemental composition of the catalysts was determined by XPS and EDS analysis, presented in table 4.1. Values for EDS differ from XPS, because EDS is very reliant on the composition of the specific particle analysed. Even though XPS is surface sensitive, it analyses a larger area of catalyst material and is, thus more reliable in terms of elemental composition. With both techniques quantification of metal content was difficult, as the signal-to-noise ratio of XP-spectra was too high to fit the spectra and in the case of EDS, the limit of determination was hit. However, it can be estimated that the total metal amount is below 0.2 at.%. Even after nitrogen doping, the majority of the catalyst consists of carbon, with single-digit amounts of nitrogen and oxygen. The carbon fraction increases after the synthesis as oxygen groups decompose but has comparable values across all catalysts. There seems to be no strong correlation between the total nitrogen content and Fe/Co ratio used in the synthesis, according to the XPS analysis.

Table 4.1: Elemental analysis in at.% by XPS and EDS.

	Carbon		Nitrogen		Oxygen	
Catalyst	XPS	EDS	XPS	EDS	XPS	EDS
Fe	92.9	95.1	3.6	2.9	3.5	1.9
FeCo(3:1)	93.4	94.3	3.7	3.8	2.9	1.8
FeCo(5:3)	94.0	95.7	4.0	2.6	2.0	1.6
FeCo(1:1)	92.8	97.2	3.8	1.2	3.5	0.9
FeCo(1:3)	93.7	90.2	3.7	4.1	2.6	5.6
Co	93.6	93.1	4.3	3.2	2.1	3.6
BP_{ox}	85.2	-	0.5	-	14.3	-

However, the total nitrogen content, bound as N-Me and N-C species, in each sample is around 3.6–4.3 at.%, which is in agreement with similar catalysts reported in the literature.[48,49] The high-resolution O1s XP-spectra can be seen in appendix figure 7.2. The carbon structures in the catalyst consist mainly of graphitic structures, as shown in C1s XP spectra exemplary for Fe-N-C and Co-N-C in comparison to BP_{ox} as reference material (figure 4.6). The remaining C1s XP spectra are displayed in appendix figure 7.1. This morphology was already observed in TEM micrographs, showing a turbostratic carbon network. About 75.9–82.5 % of the carbon species are graphitic with 4.8–9.9 % π-bound carbon and 5.0–7.8 % σ-bound carbon.

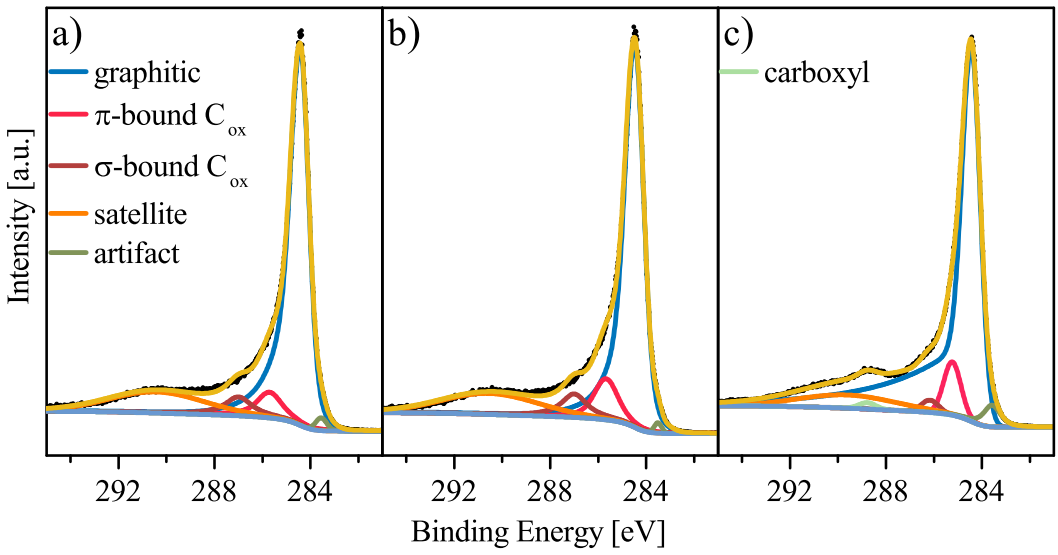

Figure 4.6: C1s high resolution XP spectra of a) Fe-N-C, b) Co-N-C and c) BP_{ox}.

Additionally, a π-π^*-satellite is visible around 290 eV with a high FWHM up to 5 eV, which is caused by π-bonding in the carbon lattice.[78] At 283 eV is an artifact noticeable that is caused by the sample holder. In the $BP_{ox.}$ reference sample is a relatively high carboxyl peak at 298 eV visible, which shrinks substantially compared to the catalyst samples, suggesting these groups get decomposed during the heat treatment.

Nitrogen functionalities are of high importance concerning the structure-property relationship in Me-N-C catalysts. It is suggested, metal ions have different structure-directing effects, especially in regard to nitrogen.[15,17] High-resolution N1s XP spectra of all six catalysts are displayed in figure 4.7 and the analysis and assignment of these, presented in table 4.2.

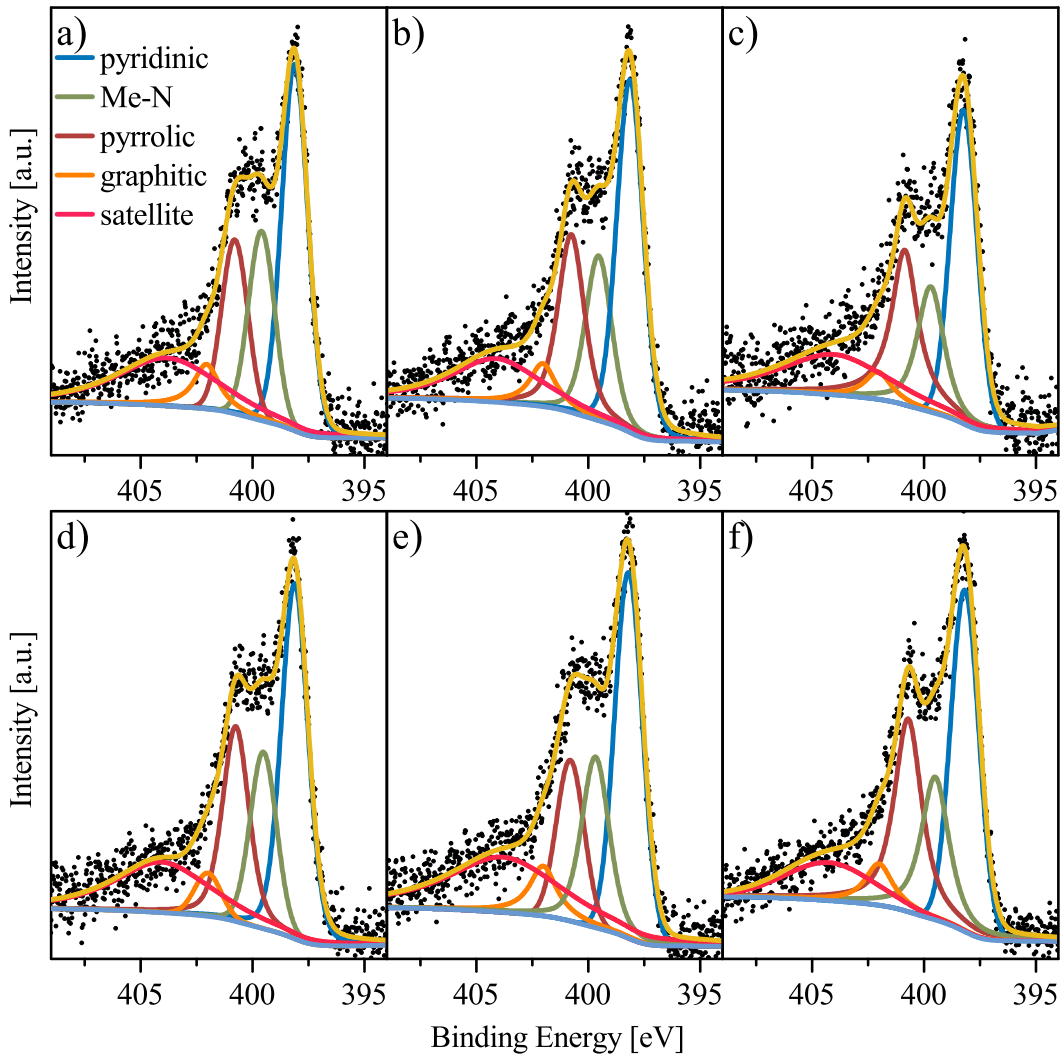

Figure 4.7: N1s high resolution XP spectra of a) Fe-N-C, b) FeCo-N-C (3:1), c) FeCo-N-C (5:3), d) FeCo-N-C (1:1), e) FeCo-N-C (1:3) and f) Co-N-C.

The signal assignment was done according to practice in literature, despite no definite consensus on each signal.[10,13,48,49] The fit parameters were kept constant throughout all samples to achieve comparability and can be seen in appendix table 7.1. A decreasing Fe/Co ratio correlates with an increase in N_x-Me fraction, indicating a higher number of nitrogen coordinated to the metal. This may be due to a higher N_x-Me density, which was reported to be the case for Co-N-C catalyst compared to Fe-N-C by Peng et al.[15] Conversely, a higher N_x-Me fraction may be caused by different coordination numbers of Co and Fe. Fe is known to be complexed by up to four nitrogen in $Fe-N_4$, $Fe-N_3$ or $Fe-N_2$ forms; however, Co was mainly reported to be coordinated fourfold and even sixfold by nitrogen.[10,15,42,44] Thus, a higher amount of N_x-Me bonds, may not be a direct proxy for more metal sites. Other nitrogen functionalities do not seem to correlate with the Fe/Co ratio at first glance; however, their property inducing effects are mainly attributed to electrochemical behavior discussed in chapter 4.3.

Table 4.2: Near-surface nitrogen functionalities in % of total nitrogen in sample, determined by XPS analysis.

Catalyst	Pyridinic	N_x-Me	Pyrrolic	Graphitic
Fe	46.9	23.5	21.8	7.8
FeCo(3:1)	46.1	22.9	26.5	7.5
FeCo(5:3)	48.6	24.0	33.8	5.9
FeCo(1:1)	48.0	23.2	28.5	5.6
FeCo(1:3)	47.5	25.4	20.9	8.9
Co	49.2	26.3	36.3	8.4

4.3 Electrochemical Activity, Selectivity and Stability of Mono- and Bimetallic Me-N-C

In the following chapter the electrochemical properties of synthesised Me-N-C catalysts will be evaluated and discussed. ORR curves and calculated parameters like activities and selectivities and the changes thereof after the AST will be assessed.

Electrochemical characterisation of the six Me-N-C catalysts was carried out in two stages. First, an initial characterisation to determine the impact of different metal ratios in the ORR performance and electrochemical properties was performed, and then a second characterisation after an AST was carried out to evaluate the stability of the catalyst. During the initial characterisation all catalysts showed a lack in reproducibility because the recorded data for each catalyst partly varied substantially. However, acknowledging the data variances, the electrochemical characterisation was carried out three times per catalyst and the data averaged and presented with its standard deviation, which is often reported in literature.[79]

4.3.1 Initial Catalyst Characterisation

ORR curves for each catalyst during the initial characterisation with indicated error bars and in relation to a Pt/C Hispec 4000 reference catalyst are shown in figure 4.8. All synthesised catalysts show lower current densities than the Pt/C reference catalyst, with the exception of Fe-N-C, which reaches similar current densities at very low potentials below 0.15 V. Considering the onset potential, all curves could be divided into two groups, those with a Fe content of more than 50 % (> 0.81 V) and less (< 0.80 V). As expected the pure Fe catalyst shows the highest current densities throughout the potential range with the highest onset potential as well as a substantially higher mixed limited and diffusion-limited current densities. The data variation was also fairly small compared to other catalysts. A linear trend between a decrease in current densities and decreasing content could however not be observed. Even though the error bars for FeCo-N-C (3:1) FeCo-N-C (5:3) are large enough to cover the average curve of each other, FeCo-N-C (5:3) shows higher current densities in the mixed limited area between ca. 0.65 and 0.75 V. In the diffusion-limited area, both catalysts show similar current densities.

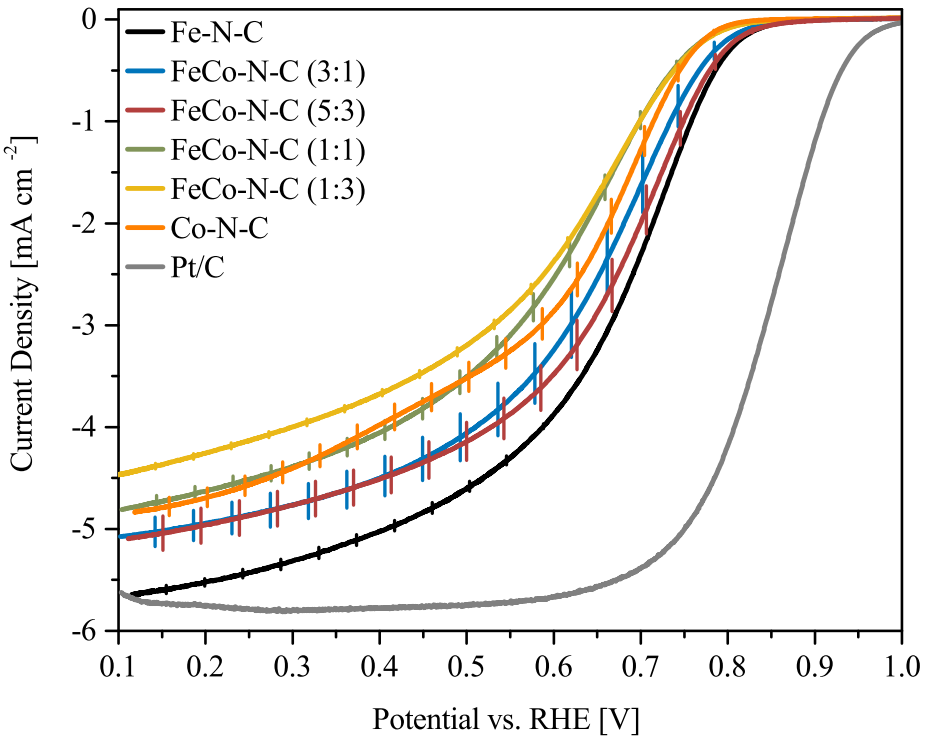

Figure 4.8: ORR curves of synthesised catalyst during the initial characterisation with commercial Pt/C Hispec 4000 reference catalyst at a Pt loading of 20 µg cm^{-2}.

Differences in the diffusion-limited area can be due to small deviations in the catalyst ink application, as pore networks differ and electrolyte mass transport is hindered. Additionally, a lower 4^- ORR selectivity and a higher resulting peroxide production could lower the diffusion-limited current density.[13,80] Despite a higher presumed kinetic activity, a lower selectivity could result in similar current densities in this area at the level of FeCo-N-C (3:1), which can be observed. The two catalysts with the lowest current densities in the mixed limited area are FeCo-N-C (1:1) and FeCo-N-C (1:3) with Co-N-C actually showing higher current densities than those two. This would suggest high amounts of Co in bimetallic FeCo-N-C catalysts lead to lower current densities compared to pure Co catalysts. In the diffusion-limited area Co-N-C produces similar current densities to FeCo-N-C (1:1), indicating again, a different ink morphology or a lower 4^- ORR selectivity comparable to the differences between FeCo-N-C (3:1) and FeCo-N-C (5:3). FeCo-N-C (1:3) shows the lowest current densities for both limited areas, suggesting the lowest kinetic activity and simultaneously mass-transport hindrance or lower 4^- ORR selectivity in relation to FeCo-N-C (1:1).

The mass activity of catalysts was determined using the current density at 0.75 V and plotted with the half-wave potential against the Fe fraction in figure 4.9. A differentiation into two groups of catalysts in the disk ORR curves is apparent again, with a sharp decrease in both parameters and especially mass activity, under 50 % Fe.

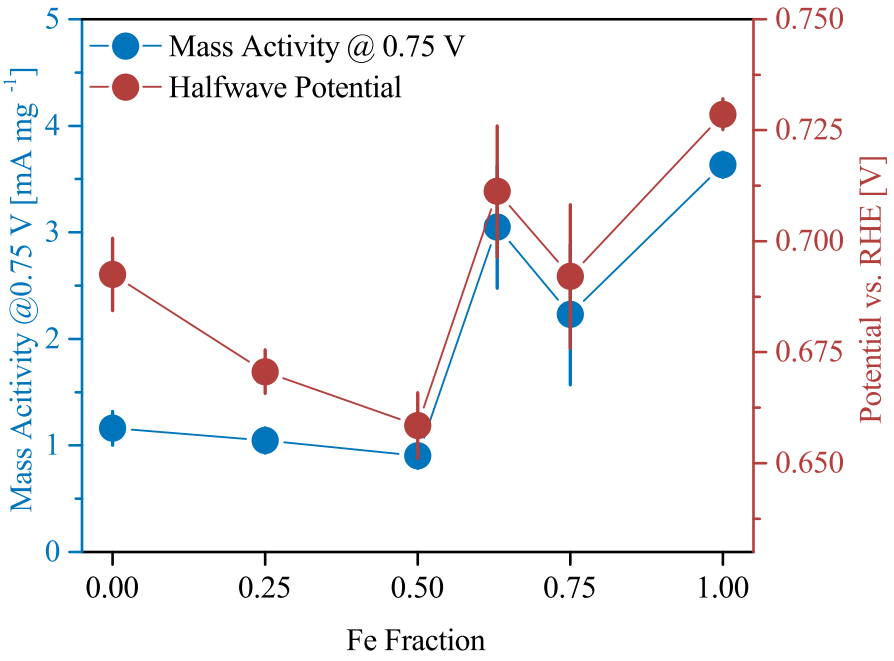

Figure 4.9: Mass activity at 0.75 V (blue) and half-wave potential (red) in relation to Fe ratio in synthesis.

The mass activity and half-wave potential follow the same trend regarding the Fe/Co ratio with similar differences between values over 50 % Fe. Fe-N-C shows the highest mass activity and half-wave potential out of all catalysts, as expected. Remarkably, FeCo-N-C (5:3) displays a substantially higher mass activity and half-wave potential than expected, almost reaching those of Fe-N-C. The non-linear trend between FeCo-N-C (5:3), FeCo-N-C (3:1) and Fe-N-C) may be due to synergistic property combinations between Fe and Co. The differences between subsequent mass activity values deviate from those of the half-wave potential at lower Fe fractions than 50 %. After a minimum at FeCo-N-C (1:1), the half-wave potential increases more extensively than the mass activity towards lower Fe fractions. This catalyst seems to have the lowest kinetic activity, as seen in the ORR curves. The error bars for this catalyst are also quite small indicating high reliability of these results. Previous work by Martinaiou et al. shows the average value of mass activity between pure Fe and pure Co catalysts for the bimetallic FeCo-N-C (1:1).[13] This could not be replicated here, as FeCo-N-C (1:1) demonstrates

lower activity and half-wave potential than its monometallic Co counterpart. Even without Fe present in the synthesis Co-N-C performs better than both catalysts with less than 50 % Fe. Additionally, comparing Co-N-C with FeCo-N-C (3:1) they show similar half-wave potential values but a substantially lower activity for Co-N-C. This could be due to the lower diffusion-limited current density and thus presumed lower $4\,e^-$ ORR selectivity compared to catalysts with 50 % Fe and more.

In comparison to other Fe-N-C catalysts, the one made here is mid-range half-wave potential-wise.[5,48] It performs adequately even compared against catalysts made from MOF structures and other synthesis methods. Moreover, bimetallic catalysts demonstrate lower mass activity and half-wave potential values but still as high as some other monometallic Fe-N-C catalysts in literature.[5]

The selectivity of the six synthesised catalysts was investigated by the evaluation of the ring current. Recorded ring current densities for each catalyst in relation to the Pt/C reference can be seen in figure 4.10. The current densities lower than 0.7 V, increase with the decrease of Fe/Co ratio.

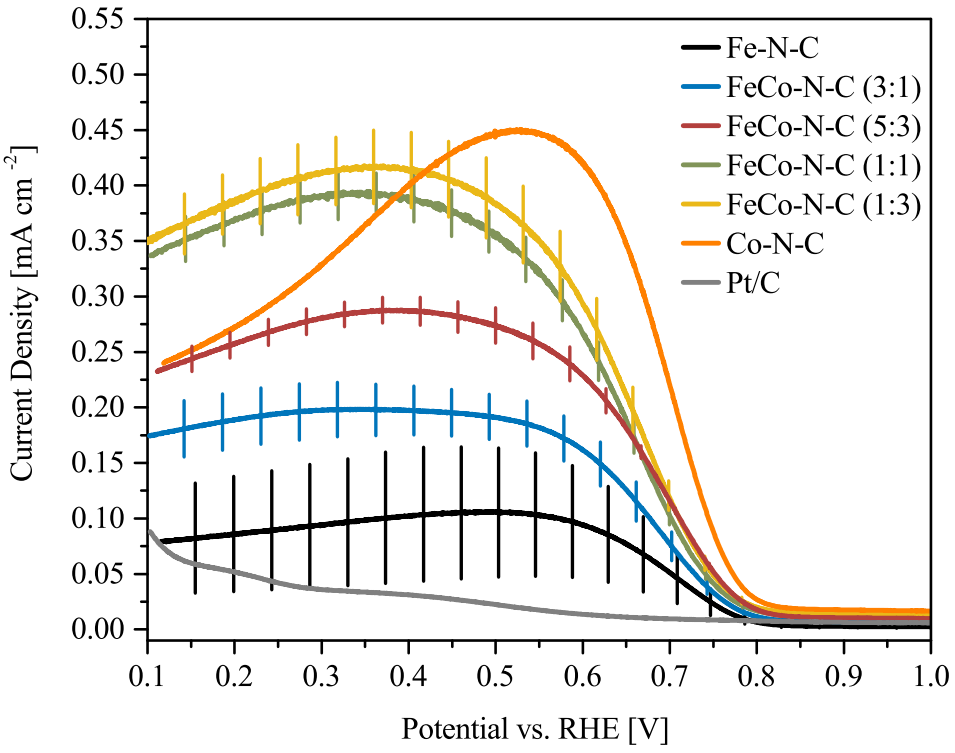

Figure 4.10: Ring current density during ORR measurement of synthesised catalyst during the initial characterisation with commercial Pt/C Hispec 4000 reference catalyst at a Pt loading of 20 µg cm^{-1}.

Therefore, an increase in Co content in the catalysts seems to increase the ring current density and thus the peroxide yield. This was reported previously as Co tends to form more H_2O_2 compared to Fe in Me-N-C catalysts.[42,43] Interestingly, with higher Co content the curve also exhibits an intensifying maximum at different potentials. For Co-N-C no error bars are shown, because the ring current density measurement in the characterisation of Co-N-C failed in two of three measurements, questioning the reliability of the data. Fe-N-C shows almost constant current densities below a potential of 0.6 V, whereas Co-N-C displays a maximum around 0.5–0.6 V with a subsequent decrease by almost half. Additionally, the ring current density of Co-N-C shows a higher potential starting point and a steeper slope than the other catalysts indicating a higher peroxide yield at higher potentials and a fast increase with lower potentials.

The peroxide yield and electron transfer number serve as an indication of the ORR mechanism selectivity. Both parameters were calculated from the ring current density in relation to the disk current density and are displayed in figure 4.11. Both parameters are calculated from the sum of the current density values below a potential of 0.75 V, which leads to a convolution of ring ORR curve features, like the maximum in current density for Co-N-C. It is suggested that Co leads to a higher peroxide yield and lower electron transfer number as the $2\,e^-$ mechanism is favoured.[42]

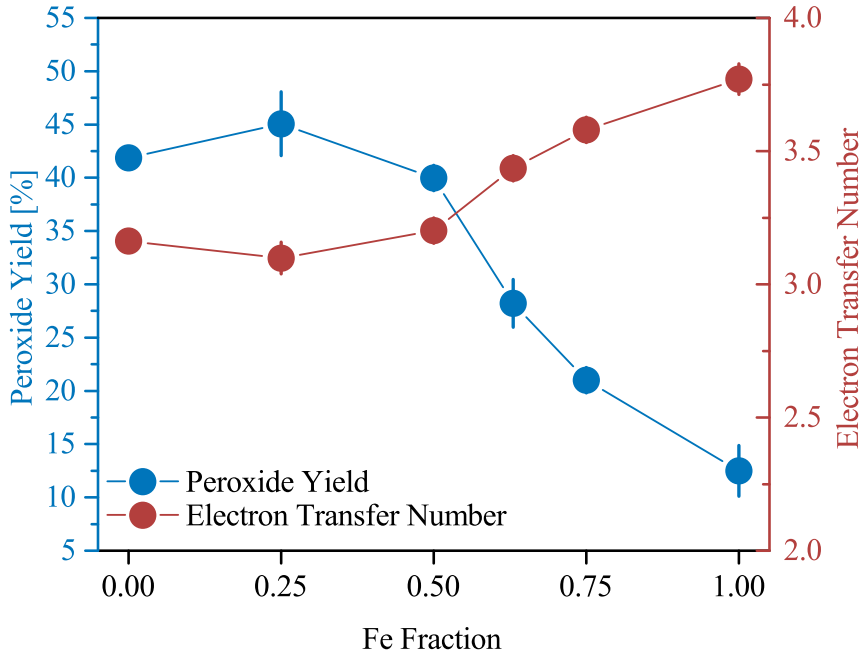

Figure 4.11: Calculated peroxide yield (blue) and electron transfer number (red) in relation to Fe ratio in synthesis.

Fe-N-C demonstrates the lowest peroxide yield electron transfer number out of all catalysts with both parameters increasing and decreasing linearly with higher Co content up to 50 %, respectively. Co-N-C and FeCo-N-C (1:3) show similar values compared to FeCo-N-C (1:1) for both peroxide yield and electron transfer number. The selectivity inducing effects of Co seem to stagnate after an amount of 50 % in the sample. Values for these parameters may be deceptive, because the formed H_2O_2 could react inside the carbon pore network and can not reach the ring to be reduced and recorded.[80] This may be problematic especially for high peroxide yield values. The increase in peroxide yield can however be an indication to an actual increase in Co content for catalysts up to 50 % Fe. Especially FeCo-N-C (5:3) shows a high mass activity, in spite of a lower selectivity compared to catalysts with more Fe content. Higher peroxide yield may however be detrimental to long-term stability, as the H_2O_2 degrades the carbon support and subsequently active sites embedded in it. Additionally, H_2O_2 created during ORR on an active Co-N-C site can induce the Fenton reaction, which forms oxygen radicals and further degrade the catalyst.[42,43]

The Tafel plots for all six catalysts are shown in figure 4.12 and display similar curve shapes for each.

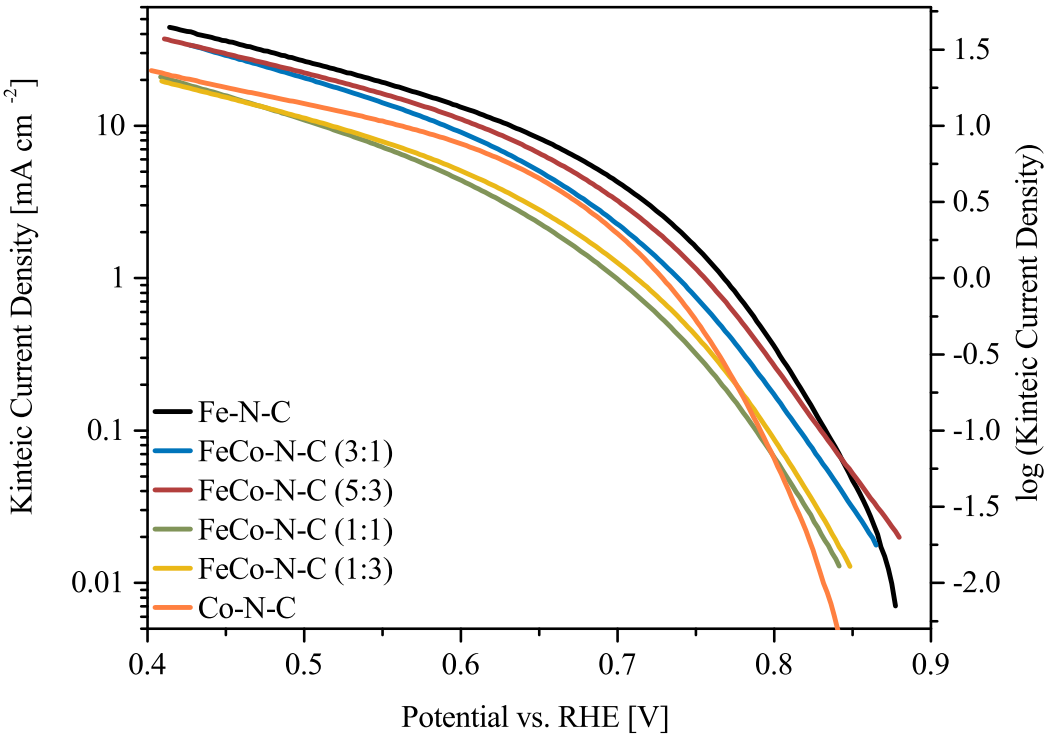

Figure 4.12: Tafel plot of all Me-N-C catalysts.

Although shifted slightly in potential, all curves are in the same potential and current density are with slight variations in the slope in the are above 0.75 V. This indicates a similarity of kinetic properties throughout all of these catalysts.[13] The Tafel slopes range from 57–83 mV dec^{-1} with bimetallic catalysts showing higher values (72–83 mV dec^{-1}) compared to monometallic ones (57–63 mV dec^{-1}). These values are in agreement with ones reported in literature for similar catalysts.[15,48] A lower Tafel slope of Co-N-C compared to Fe-N-C was also observed by Peng et al., despite lower mass activity and higher peroxide yield.[15]

4.3.2 Accelerated Stress Test Induced Catalyst Changes

The stability of Me-N-C catalysts is an important criteria, since LT-PEMFC have to operate for prolonged time without a performance loss exceeding 5 % over its live span according to the U.S. DOE.[6] The stability test carried out in this work is adapted from the Fuel cell conference of Japan (FCCJ) and Martinaiou et al. and focuses primarily on carbon corrosion during start-stop procedures, which induce high potentials.[6,13,68] The AST was performed with cyclic voltammetry in a potential window from 1.0 to 1.5 V in 5000 cycles in nitrogen saturated electrolyte. At potentials over 1.0 V, carbon is electrochemically oxidised in acidic media and can become unstable.[81] Furthermore, due to the oxidation of the carbon matrix, embedded active Me-N-C sites and nitrogen moieties can degrade and subsequently diminish the catalysts activity.[13] Cyclic voltammograms of the six synthesised catalysts before and after the AST can be seen in figure 4.13. Before the AST there does not seem to be a peak present, just capacitive currents, which depend on the surface area and thus on the morphology and homogeneity of the catalyst ink. The amount of capacitance throughout all samples varied considerably, even within measurements of the same catalyst. A correlation of capacitance and Fe/Co ratio could not be established due to the heterogeneity of each sample. Additionally, no redox peak stemming from Fe or Co are visible, these would appear at potentials of 0.75 V and 1.25 V, respectively.[42] After the AST there is a significant peak visible across the whole potential window. This can be assigned to quinone/hydroquinone functionalities normally occurring around 0.6–0.7 V.[82,83] An increase in capacitive currents with the AST can thus not be evaluated from CV, since the quinone/hydroquinone peak is broadened to the whole width of the potential range. Oxidation of carbon can be detected through CV at the redoxactive quinone/hydroquinone peak.[82,83]

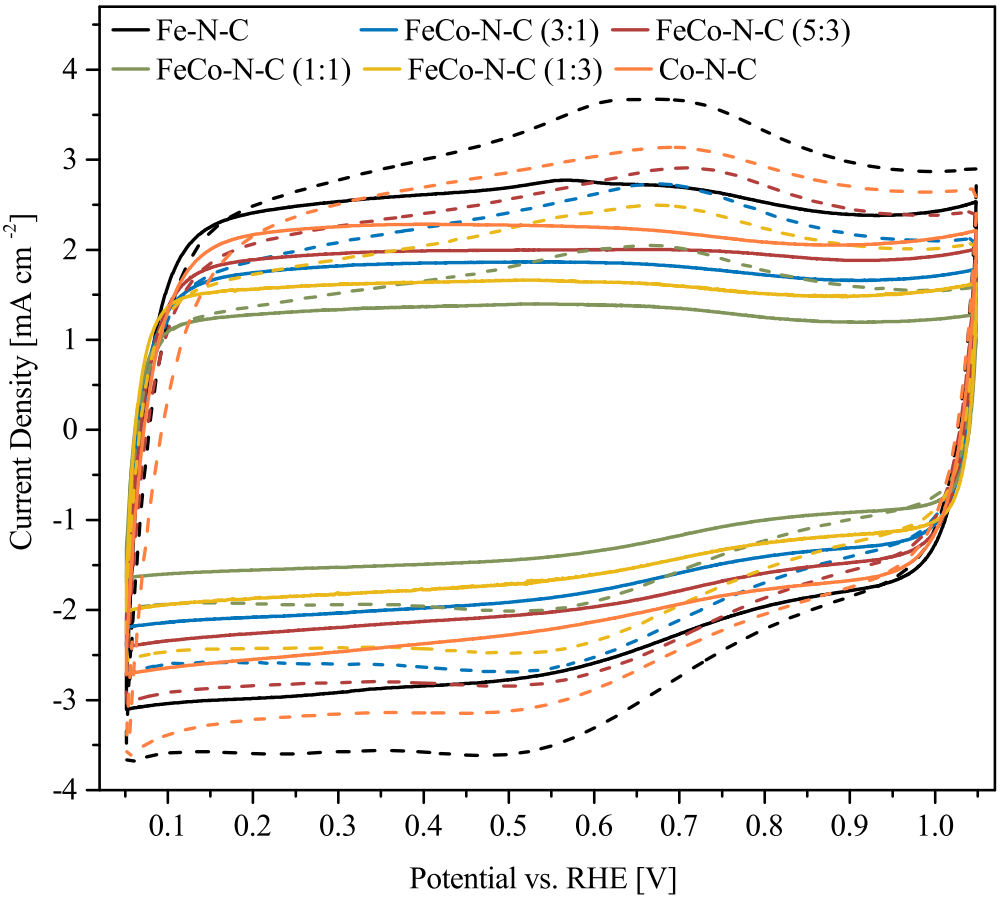

Figure 4.13: Comparison of CV before (full) and after (dashed) the AST of all six catalysts.

The sharp increase of this peak indicates that the carbon was substantially oxidised. However, this peak is not a quantitative measure for carbon oxidation, since carbon can be fully oxidised to CO_2, which leaves the structure and is no longer redox-active.

The capacity variance under different voltammetry scan rates can be a measure for the electrochemically accessible area.[84] Linear sweep voltammetry is carried out in an non-farradaic area (figure 4.14a) and the current density at a fixed potential plotted against the sweep rate (figure 4.14b). The slope of the resulting ideally linear graph is the capacity. Values for all catalysts except Fe-N-C, where no data was available, are presented in table 4.3. Song et al. reported a positive relationship of capacitance and electrochemically active surface area, however no clear correlation was possible between the ORR performance and capacitance of the synthesised catalysts.[84]

The differences in capacitance could also be due to inhomogeneity of the catalyst ink. Catalysts with up to 50 % Fe content follow the trend of higher capacity resulting in

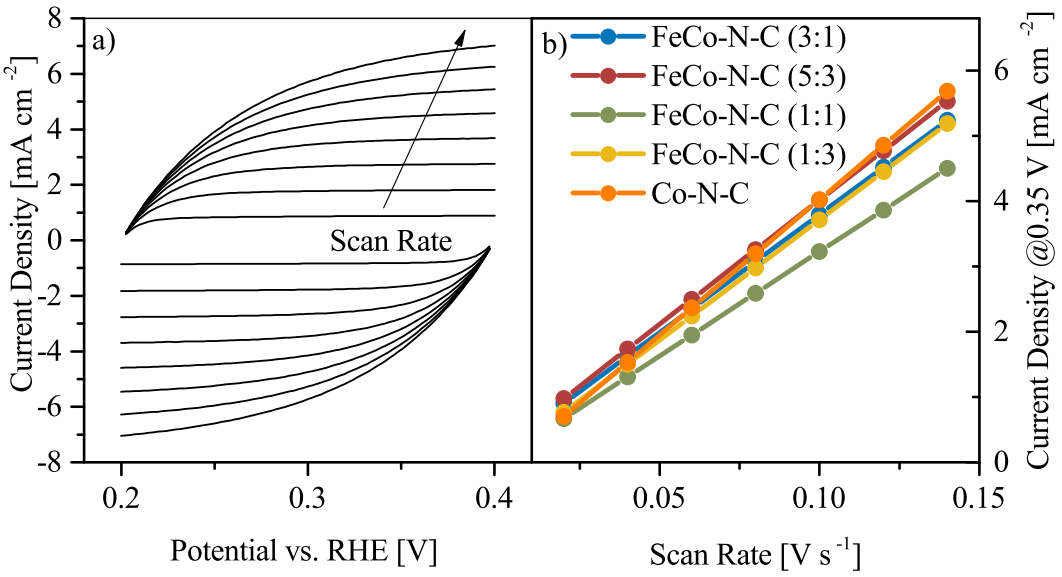

Figure 4.14: a) Exemplary sweep voltammetry of FeCo-N-C (5:3) forward (upper) and backward (lower) scan at different scan rates between 0.02 and 0.14 V s^{-1} and b) linear fit and slope extraction of the current density at 0.35 V against the scan rate.

higher activity, but FeCo-N-C (3:1) shows a lower capacitance than FeCo-N-C 1:3, despite a substantially higher activity. All catalysts show about the same increase in capacitance after the AST with only small differences of about 3 % between the highest and lowest increase, which however do not coincide with any other metric. The increase in capacitance through carbon oxidation across all catalysts is about 10 %, which is not surprising considering, all catalysts consist of about 90 % carbon. Oxidation can increase the available surface area of the support through changes of the pore network,

Table 4.3: Capacitance values before and after AST with percentage increase for all catalysts, except Fe-N-C.

Fe/Co Ratio	Mass Activity [mA mg^{-1}]	Capacity Before AST [mF cm^{-2}]	Capacity After AST [mF cm^{-2}]	Increase [%]
3:1	2.2	32.8 ± 10.5	36.1 ± 11.0	10.3
5:3	3.0	35.0 ± 5.3	38.0 ± 5.5	8.6
1:1	0.9	29.4 ± 1.9	32.0 ± 1.7	8.6
1:3	1.0	33.2 ± 0.0	36.9 ± 0.0	11.2
0:1	1.2	37.6 ± 1.8	41.5 ± 2.0	10.4

but an oxygenation of the surface also increases the capacitance as shown by Hsieh et al.[85] Not only leads the oxidation of carbon to different capacities, there is also evidence carbon basicity increases ORR activity and the surface oxidation may, thus reduce the basicity, hence the ORR activty.[81,86]

The catalysts ORR activity decreases during the AST, as seen in figure 4.15, but the decrease varies with the Fe/Co ratio.

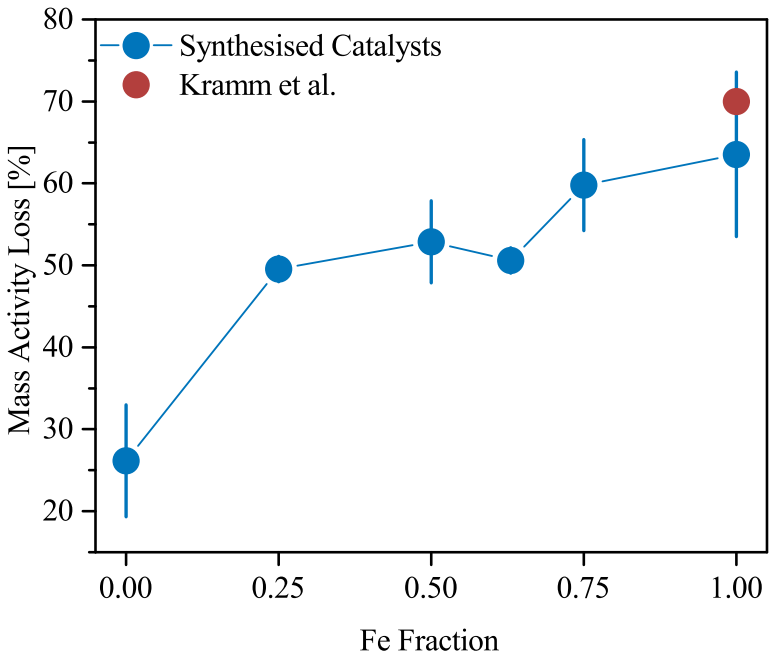

Figure 4.15: Loss of mass activity after the AST in relation to Fe fraction in synthesis of all synthesised catalysts (blue) and reference catalyst with a similar synthesis from Kramm et al.[82] (red).

The activity loss is highest in Fe-N-C and decreases with increasing Co content. Remarkably, the mass activity loss decreases significantly in monometallic Co-N-C in comparison to the visible trend. Co is suggested to enhance the stability of the resulting catalyst, hence it is no surprise that catalyst with increasing Co content show a better stability.[43,50] The presence of Fe, even small amounts of 25 % Fe, may render the catalyst more prone to degradation through carbon corrosion. Regarding mass activity and half-wave potential, FeCo-N-C (5:3) showed diverging behavior from the observed trend. In terms of mass activity loss, FeCo-N-C (5:3) shows lower than expected values. Additionally, the error bars for this catalyst are also quite low in comparison to those with higher Fe amounts, suggesting a persistently lower degradation character. It could be argued that high Fe content catalysts degrade faster, due to their higher initial activity.

The correlation of initial activity to activity loss however does not endure, because the about 10–15 % lower activity loss for FeCo-N-C (1:1) and FeCo-N-C (1:3) compared to Fe-N-C does not relate to the 65 % lower initial activity, for the same catalysts.

The change of onset and half-wave potentials after AST, shown in figure 4.16 attest to the activity and stability of the catalysts. For both potentials a decrease can be observed after AST, depending on the catalysts. Apparently, the half-wave potential decreases more than the onset potential for all catalysts except Co-N-C. This difference could be due to different degradation effects becoming evident at the potential areas of these parameters. The onset potential is mainly attributed to the kinetic limited current density area, which represents the intrinsic catalytic activity of the active sites.[55] Lower onset potentials could thus be evidence for a lower amount of active sites, caused by their degradation during the AST.

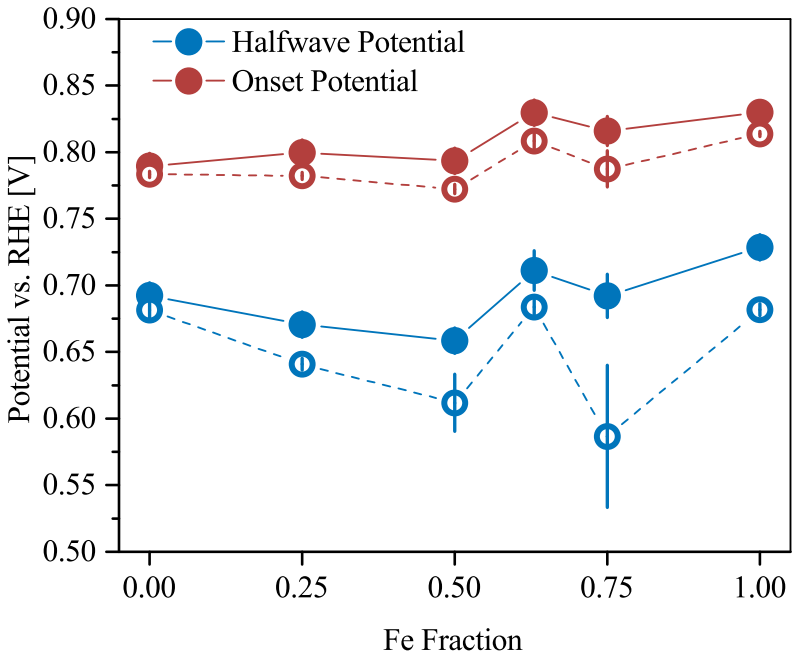

Figure 4.16: Onset and half-wave potential before (full) and after (dashed) the AST in relation to Fe content in synthesis.

Since there are different ORR active sites present in Me-N-C catalysts, higher degradation of specific sites can change their ratio and consequently changing the onset potential. The onset potential change is higher for bimetallic catalysts (2.3–3.5 % loss) compared to monometallic ones (0.8–1.9 % loss) but still quite small compared to the mass activity loss differences between catalysts. Differences between bimetallic and monometallic catalysts could be due to a interaction of different sites in the bimetal-

lic catalysts. The half-wave potential change may be caused by effects predominantly arising from mass transport phenomena, as in this mixed limited current density area mass transport effects as well as kinetic effects transpire and the onset potential change as an indication for kinetic differences is smaller in comparison.[12,55] Considering the half-wave potential change, the bimetallic catalysts also show higher decrease compared to monometallic ones with the exception of FeCo-N-C (5:3), which displays a relatively small change. FeCo-N-C (5:3) again shows, relatively superior stability, only exceeded by the monometallic Co-N-C. Especially in combination with the initial fairly high half-wave potential such a small change is remarkable. The smallest change attributed to Co-N-C, may be caused by the structure inducing effects of Co, stabilising the carbon support and thus reducing increased mass-transport hindrance caused by degradation.[15]

The changes in ORR selectivity considering the peroxide yield and electron transfer number are displayed in 4.17. Evidently, the selectivity decreases across all catalysts for both parameters with the exception of the monometallic Fe-N-C and Co-N-C catalysts. These catalysts do not seem to show an increase peroxide yield after the AST and Co-N-C even shows a decrease. The electron transfer number however shows a slight decrease for Fe-N-C and Co-N-C seems to have improve $4\,e^-$ ORR selectivity after the AST. Furthermore, the loss in $4\,e^-$ selectivity seems to increase with increasing Co content in the bimetallic catalysts, most visible in the peroxide yield.

Consequently, the peroxide yield increases the most for FeCo-N-C (1:3) to almost 60 %. Sparse $Fe-N_x$ sites in the high Co content catalysts may degrade preferably than Co sites; therefore, reducing the $4\,e^-$ ORR selectivity even further. Even though the stability in terms of mass activity, onset and half-wave potential remarkably high for FeCo-N-C (5:3), its peroxide yield increases proportionally more with the AST. The proposed stability inducing effects of Co can be seen in all catalysts in terms of lower mass activity loss, ergo higher Co content leads to higher retention of initial mass activity. However, the catalysts degradation behavior cannot be linearily correlated to Co content. In terms of mass activity loss, monometallic Co-N-C is substantially more prone to degradation and regarding onset and half-wave potential even Fe-N-C shows lower potential loss than bimetallic catalysts. Martinaiou et al. suggested that bimetallic catalysts degrade stronger than their monometallic counterparts, however this could not have been confirmed, since there is much more variation in relation to the Fe/Co ratio in carbon corrosion stability between different bimetallic catalysts.[13]

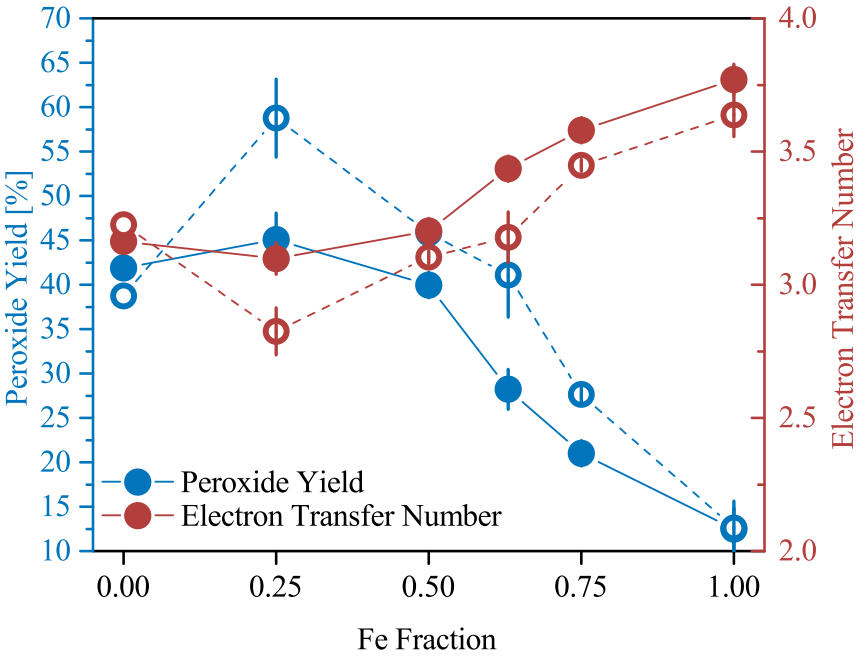

Figure 4.17: Changes in peroxide yield and electron transfer number before (full) and after (dashed) the AST.

Especially, the ratio of Fe/Co 5:3 seems to induce relatively much more corrosion resistance, with simultaneous high activity.

4.4 Influence of the Fe/Co Ratio Structural Properties in Relation to Electrochemical Behavior

The ratio of Fe/Co used in the synthesis of Me-N-C influences their morphology and electrochemical properties as seen in previous chapters. Hereinafter, the relationship between the structure and chemical composition of the catalyst with electrochemical behaviour will be evaluated.

Even though the differences in fraction of nitrogen functionalities to total nitrogen show a marginal a correlation can be seen between the pyridinic nitrogen and mass activity loss of the catalysts after the AST. This relationship can be seen in figure 4.18.

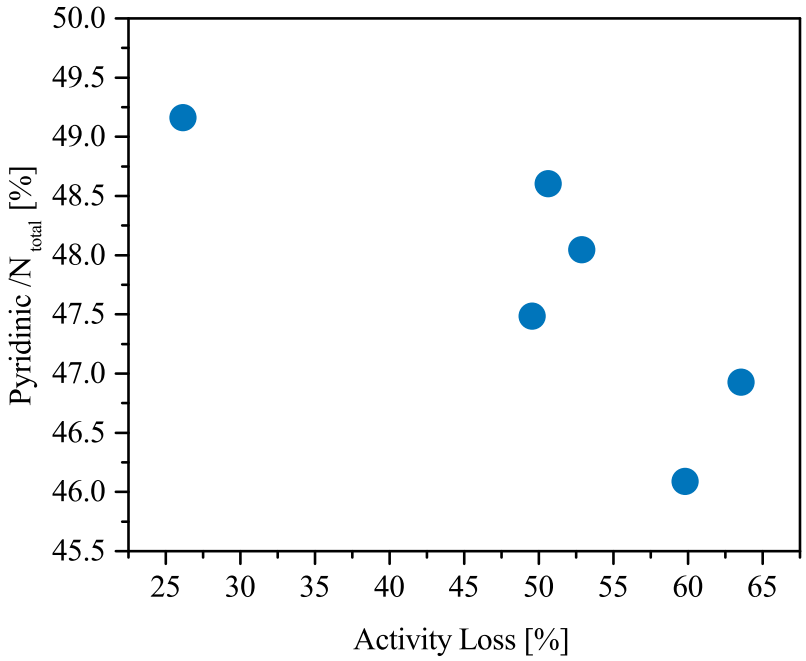

Figure 4.18: Pyridinic nitrogen as fraction of total nitrogen content in relation to the mass activity loss after the AST.

Pyridinic nitrogen is supposedly ORR active, for the reduction of H_2O_2 to H_2O and thus coultd protect the catalyst from carbon corrosion induced by peroxides.[10,81] Peroxide formation does however not occur substantially during the performed AST under nitrogen saturated electrolyte, hence a further corrosion retardation by pyridinic nitrogen is possible under operation conditions.

A correlation by pyrrolic nitrogen and the peroxide yield was reported in literature, but no such relation ship could be observed in the synthesised catalysts.[10] Even though FeCo-N-C (1:3) shows a high peroxide yield, its pyrrolic nitrogen was the lowest out of all. Since the pyridinic/pyrrolic ratio is quite high for the synthesised catalyst, formed peroxide could be further reduced by pyridinic nitrogen before being detected at the ring. The addition of Co to Fe-N-C catalysts could be advantageous. As shown, a Fe/Co ratio of 5:3 seems to improve the stability of the catalyst with concurrent high mass activity and half-wave potential. However, an increased peroxide yield and lower electron transfer number compared to Fe-N-C could be detrimental to long-term stability under fuel cell operation conditions. Low amounts of Co content, namely 25 and 50 % do not have advantageous effects, but are rather detrimental. These catalysts show lower mass activity compared to Co-N-C with lower stability and $4\,e^-$ ORR selectivity. Thus the use of monometallic Co-N-C catalysts is beneficial compared to bimetallic FeCo-N-C (1:1) and FeCo-N-C (1:3).

5 Conclusions and Outlook

The goal of this thesis is to provide a systemic approach to the evaluation of the influence of different ratios of metal in bimetallic FeCo-N-C electrocatalysts. In total six different mono- and bimetallic catalysts with differing Fe/Co ratios were synthesised and investigated with physical and electrochemical characterisation techniques. The catalysts show a homogenoues distribution of both metals across the catalyst, as evidenced through EDS elemental mapping. Agglomerations of metal, indicating metal particles are visible in all catalysts. No detection of metal particles was possible with XRD or XPS, suggesting the amount of particles formed is quite low in comparison to previously reported catalysts in literature.[17,75] The elemental composition regarding carbon, nitrogen and oxygen of all six catalysts is in agreement with similar catalysts.[48,49] Nitrogen containing functional groups do not seem to correlate with the Fe/Co ratio, with the exception of the proposed $Me-N_x$ group, which increases in relation to the total nitrogen content with increasing Co content used in the synthesis.

The synthesised catalysts show a low reproducibility during electrochemical characterisation with data of multiple measurements of the same catalyst varying. Nonetheless, different electrochemical properties depending on the Fe/Co ratio can be observed. The ORR performance in terms of mass activity and half-wave potential of the catalysts seems to decrease with increasing Co content up to 50 % Co, with the exception of FeCo-N-C (5:3), which shows a performance exceeding FeCo-N-C (3:1). Below 50 % Fe, the ORR performance increases again with the monometallic Co-N-C displaying better mass activity and half-wave potential than FeCo-N-C (1:1) and FeCo-N-C (1:3). The $4\,e^-$ ORR selectivity also seems to decrease with increasing Co content up to 50 % Co, after which it stagnates. Even though FeCo-N-C (5:3) showed exceptional performance, its selectivity follows the linear trend, mentioned. For stability evaluation the catalysts were exposed to an AST. All six catalysts show a decrease in mass activity loss after the AST with increasing Co content, with Co-N-C displaying exceptional stability compared to the other catalysts. This stability enhancement seems to correlate with the pyridinic nitrogen content in the catalysts. The half-wave potential shows a higher decrease than the onset potential after the stress test, suggesting a higher influence of mass-transport hindrance compared to kinetic activity. This can be elaborated by an evident carbon corrosion after the AST, as evidenced by an significant increase quinone/hydroquinone

functionalities in cyclic voltammograms. A corrosion of carbon can additionally be presumed through an capacitance increase of about 10 %. The $4\,e^-$ ORR selectivity of the catalysts decreases stronger in bimetallic compared to monometallic ones. In fact, monometallic catalysts show no increase in peroxide yield after the AST, with Co-N-C even decreasing in yield. These results suggest a possible trade-off of stability and performance, with FeCo-N-C (5:3) showing high stability with concurrent high performance. Low amounts of Fe below 50 % however display a low ORR performance even compared to monometallic Co-N-C catalysts without an improvement in stability or selectivity.

In further investigations the stability improvement of the addition of Co to Fe-N-C catalysts could to be studied in different AST conditions. Besides the start-up and shut-down AST conditions, a load cycle AST could be done with the focus on degradation of metal sites in a potential window of 0.0–1.0 V vs. RHE.[13,82] It was already reported, that an AST under oxygen saturated electrolyte in a potential window of 0.0–1.0 V vs. RHE increases the degradation manyfold compared to inert gas saturation, because of the production of H_2O_2 during the AST.[87] The increased production of H_2O_2 with rising Co content and subsequent degradation thus may have the consequence of increased degradation. This is of special importance since H_2O_2 can be converted to reactive radicals through the Fenton reaction and thus a higher peroxide yield with the addition of Co may be detrimental to the stability.[81,87] Furthermore, the impact of an increased peroxide yield compared to monometallic Fe-N-C needs to be investigated in regards to fuel cell operation and its long-term stability. An elucidation of the active sites in bimetallic Me-N-C with techinques like EXAFS and XANES could find reasons for the exceptional behavior of FeCo-N-C (5:3). In this regard, the determination of the actual metal content and ratio in the synthesised catalysts could be pivotal. Finally, the investigation of bimetallic catalysts could be extended to other synthesis methods, namely to determine whether similar effects can be observed in different catalysts.

6 Bibliography

[1] F. M. Orr, *ACS Energy Lett.* **2016**, *1*, 113–114.

[2] T. P. Senftle, E. A. Carter, *Acc. Chem. Res.* **2017**, *50*, 472–475.

[3] F. Zhang, P. Zhao, M. Niu, J. Maddy, *Int. J. Hydrogen Energy* **2016**, *41*, 14535–14552.

[4] F. Jaouen, D. Jones, N. Coutard, V. Artero, P. Strasser, A. Kucernak, *Johnson Matthey Technol. Rev.* **2018**, *62*, 231–255.

[5] L. Osmieri, *ChemEngineering* **2019**, *3*, 16.

[6] R. Borup et al., *Chem. Rev.* **2007**, *107*, 3904–3951.

[7] M. Suha-Yazici, H. A. Yavasoglu, M. Eroglu, *Int. J. Hydrogen Energy* **2013**, *38*, 11639–11645.

[8] G. Wu et al., *J. Mater. Chem.* **2011**, *21*, 11392–11405.

[9] A. Wilson, G. Kleen, D. Papageorgopoulos, DOE Hydrogen and Fuel Cells Program Record 17007- Fuel Cell System Cost-2017, Report, US Department of Energy, **2017**.

[10] K. Artyushkova, A. Serov, S. Rojas-Carbonell, P. Atanassov, *J.Phys. Chem. C* **2015**, *119*, 25917–25928.

[11] H. T. Chung, D. A. Cullen, D. Higgins, B. T. Sneed, E. F. Holby, K. L. More, P. Zelenay, *Science* **2017**, *357*, 479.

[12] J. H. Zagal, F. Bedioui, *Electrochemistry of N4 Macrocyclic Metal Complexes: Volume 1: Energy*, 2nd ed., Springer International Publishing, Cham, **2016**.

[13] I. Martinaiou, A. Shahraei, F. Grimm, H. Zhang, C. Wittich, S. Klemenz, S. J. Dolique, H.-J. Kleebe, R. W. Stark, U. I. Kramm, *Electrochim. Acta* **2017**, *243*, 183–196.

[14] H. M. Barkholtz, D.-J. Liu, *Mater.Horiz.* **2017**, *4*, 20–37.

[15] H. Peng et al., *ACS Catal.* **2014**, *4*, 3797–3805.

[16] G. Wu, K. L. More, C. M. Johnston, P. Zelenay, *Science* **2011**, *332*, 443–459.

[17] V. Nallathambi, J.-W. Lee, S. P. Kumaraguru, G. Wu, B. N. Popov, *J. Power Sources* **2008**, *183*, 34–42.

[18] J. Zhang, *PEM Fuel Cell Electrocatalysts and Catalyst Layers*, Springer, London, **2008**.

[19] Z. Sun, J. Pan, J. Guo, F. Yan, *Adv. Sci.* **2018**, *5*, 1800065.

[20] A. Serov, I. V. Zenyuk, C. G. Arges, M. Chatenet, *J. Power Sources* **2018**, *375*, 149–157.

[21] J. Mulot, S. Jemei, M.-C. Péra, B. Jeanneret, J.-M. Kauffmann, Dynamic and environmental performance of Solid Oxide Fuel Cell systems fed with natural gas and diesel fuel, Conference Paper, **2011**.

[22] Q. Li, D. Aili, H. A. Hjuler, J. O. Jensen, *High Temperature Polymer Electrolyte Membrane Fuel Cells - Approaches, Status, and Perspectives*, 1st ed., Springer International Publishing, Switzerland, **2016**, p. 545.

[23] J. H. Zagal, F. Bedioui, J.-P. Dodelet, *N4-Macrocyclic Metal Complexes*, Springer, **2006**.

[24] R. Jasinski, *Nature* **1964**, *201*, 1212–1213.

[25] A. van-der-Putten, A. Elzing, W. Visscher, E. Barendrecht, *J. Electroanal. Chem. Interfacial Electrochem.* **1986**, *214*, 523–533.

[26] A. van-der-Putten, A. Elzing, W. Visscher, E. Barendrecht, *J. Electroanal. Chem. Interfacial Electrochem.* **1987**, *221*, 95–104.

[27] H. Jahnke, M. Schönborn, G. Zimmermann in Physical and Chemical Applications of Dyestuffs, (Eds.: F. P. Schäfer, H. Gerischer, F. Willig, H. Meier, H. Jahnke, M. Schönborn, G. Zimmermann), Springer Berlin Heidelberg, **1976**, pp. 133–181.

[28] V. S. Bagotzky, M. R. Tarasevich, K. A. Radyushkina, O. A. Levina, S. I. Andrusyova, *J. Power Sources* **1978**, *2*, 233–240.

[29] S. Gupta, D. Tryk, I. Bae, W. Aldred, E. Yeager, *J. Appl. Electrochem.* **1989**, *19*, 19–27.

[30] D. Zhao, J.-L. Shui, C. Chen, S. Comment, B. Reprogle, D.-J. Liu, *ECS Trans.* **2013**, *50*, 1861–1868.

[31] J. Shui, C. Chen, L. Grabstanowicz, D. Zhao, D.-J. Liu, *Proc. Natl. Acad. Sci. U. S. A.* **2015**, *112*, 10629–10634.

[32] W. Xia, J. Zhu, W. Guo, L. An, D. Xia, R. Zou, *J. Mater. Chem. A* **2014**, *2*, 11606–11613.

[33] K. Fujie, K. Otsubo, R. Ikeda, T. Yamada, H. Kitagawa, *Chem. Sci.* **2015**, *6*, 4306–4310.

[34] S. Shrestha, W. E. Mustain, *J. Electrochem. Soc.* **2010**, *157*, B1665–B1672.

[35] J. Zeng, C. Francia, C. Gerbaldi, M. A. Dumitrescu, S. Specchia, P. Spinelli, *J. Solid State Electrochem.* **2012**, *16*, 3087–3096.

[36] N. Probst, E. Grivei, *Carbon* **2002**, *40*, 201–205.

[37] B. Fang, N. K. Chaudhari, M.-S. Kim, J. H. Kim, J.-S. Yu, *J. Am. Chem. Soc.* **2009**, *131*, 15330–15338.

[38] G. Wu, N. H. Mack, W. Gao, S. Ma, R. Zhong, J. Han, J. K. Baldwin, P. Zelenay, *ACS Nano* **2012**, *6*, 9764–9776.

[39] Q. Li, G. Wu, D. A. Cullen, K. L. More, N. H. Mack, H. T. Chung, P. Zelenay, *ACS Catal.* **2014**, *4*, 3193–3200.

[40] H. T. Chung, P. Zelenay, Non-precious metal catalysts prepared from precursor comprising cyanamide, Patent, **2015**.

[41] H. T. Chung, J. H. Won, P. Zelenay, *Nat. Commun.* **2013**, *4*, 1922.

[42] X. X. Wang, V. Prabhakaran, Y. He, Y. Shao, G. Wu, *Adv. Mater.* **2019**, *31*, 1805126.

[43] J. Liu, Z. Jin, X. Wang, J. Ge, C. Liu, W. Xing, *Sci. China: Chem.* **2019**, *62*, 669–683.

[44] U. I. Kramm et al., *Phys. Chem. Chem. Phys.* **2012**, *14*, 11673–11688.

[45] L. Osmieri et al., *Applied Catalysis B: Environmental* **2019**, *257*, 117929.

[46] H. Schmies et al., *Chem. Mater.* **2018**, *30*, 7287–7295.

[47] S. Maldonado, S. Morin, K. J. Stevenson, *Carbon* **2006**, *44*, 1429–1437.

[48] F. Jaouen et al., *ACS Appl. Mater. Interfaces* **2009**, *1*, 1623–1639.

[49] G. Wu, P. Zelenay, *Acc. Chem. Res.* **2013**, *46*, 1878–1889.

[50] Q. Cheng, L. Yang, L. Zou, Z. Zou, C. Chen, Z. Hu, H. Yang, *ACS Catal.* **2017**, *7*, 6864–6871.

[51] A. J. Bard, L. R. Faulkner, *Electrochemical Methods: Fundamentals and Applications*, 2nd ed., John Wiley and Sons, **2001**.

[52] K. J. J. Mayrhofer, D. Strmcnik, B. Blizanac, V. Stamenkovic, M. Arenz, N. M. Markovic, *Electrochim. Acta* **2008**, *53*, 3181–3188.

[53] A. J. Bard, G. Inzelt, F. Scholz, *Electrochemical Dictionary*, 2nd, Springer, Berlin, Heidelberg, **2012**.

[54] C. M. A. Brett, A. M. O. Brett, *Electrochemistry Principles, Methods, and Applications*, Oxford University Press, New York, **1993**.

[55] A. J. Bard, M. Stratmann, P. R. Unwin, *Encyclopedia of Electrochemistry - Instrumentation and Electroanalytical Chemistry*, WILEY-VCH, Weinheim, **2003**.

[56] P. W. Atkins, J. de Paula, *Physikalische Chemie*, 4th ed., Wiley-VCH, Weinheim, **2006**.

[57] U. A. Paulus, T. J. Schmidt, H. A. Gasteiger, R. J. Behm, *J. Electroanal. Chem.* **2001**, *495*, 134–145.

[58] J. F. Watts, J. Wolstenholme, *An Introduction to Surface Analysis by XPS and AES*, John Wiley and Sons Ltd., Chichester, United Kingdom, **2003**.

[59] G. Friedbacher, H. Bubert, *Surface and Thin Film Analysis: A Compendium of Principles, Instrumentation, and Applications*, 2nd ed., Wiley-VCH, Weinheim, **2011**.

[60] M. Necke, *Zersetzungsverhalten neuartiger, kohlenstofffreier Gold-Precursoren für den Einsatz in elektronenstrahlgestützten additiven Strukturierungsverfahren zur direkten Abscheidung von Metallen*, Dissertation, Carl von Ossietzky Universität Oldenburg, **2010**.

[61] D. Fenske, *Synthese, Charakterisierung und Anwendung kolloidaler Nanopartikel in der heterogenen Katalyse*, Dissertation, Carl von Ossietzky Universität Oldenburg, **2009**.

[62] J. Thomas, T. Gemming, *Analytical Transmission Electron Microscopy : An Introduction for Operators*, Springer Netherlands, Heidelberg, **2014**.

[63] R. F. Egerton, *Physical Principles of Electron Microscopy : An Introduction to TEM, SEM, and AEM*, 2nd ed., Springer International Publishing, Basel, **2016**.

[64] W. Massa, *Kristallstrukturbestimmung*, 8th ed., Springer Spektrum, Wiesbaden, **2015**.

[65] R. Guinebretiere, *X-ray diffraction by polycrystalline materials*, ISTE, London Newport Beach, CA, **2007**.

[66] C. Wei, R. R. Rao, J. Peng, B. Huang, I. E. L. Stephens, M. Risch, Z. J. Xu, Y. Shao-Horn, *Adv. Mater.* **2019**, *31*, 1806296.

[67] K. Shinozaki, J. W. Zack, R. M. Richards, B. S. Pivovar, S. S. Kocha, *J. Electrochem. Soc.* **2015**, *162*, F1144–F1158.

[68] A. Ohma, K. Shinohara, A. Iiyama, T. Yoshida, A. Daimaru, *ECS Trans.* **2011**, *41*, 775–784.

[69] J. Tian, L. Birry, F. Jaouen, J. P. Dodelet, *Electrochim. Acta* **2011**, *56*, 3276–3285.

[70] Z. Q. Li, C. J. Lu, Z. P. Xia, Y. Zhou, Z. Luo, *Carbon* **2007**, *45*, 1686–1695.

[71] M. Carmo, A. R. dos Santos, J. G. R. Poco, M. Linardi, *J. Power Sources* **2007**, *173*, 860–866.

[72] J. H. Kim, Y. J. Sa, H. Y. Jeong, S. H. Joo, *ACS Appl. Mater. Interfaces* **2017**, *9*, 9567–9575.

[73] Y. Hu, J. O. Jensen, W. Zhang, S. Martin, R. Chenitz, C. Pan, W. Xing, N. J. Bjerrum, Q. Li, *J. Mater. Chem. A* **2015**, *3*, 1752–1760.

[74] L. Chen et al., *Nanotechnology* **2013**, *24*, 045602.

[75] J.-Y. Choi, R. S. Hsu, Z. Chen, *J.Phys. Chem. C* **2010**, *114*, 8048–8053.

[76] S. Hosseinzadeh, A. Yazdani, R. Khordad, *Eur. Phys. J.: Appl. Phys.* **2012**, *59*, 30401.

[77] V. Jovic, V. Maksimovic, M. G. Pavlović, K. Popov, *J. Solid State Electrochem.* **2006**, *10*, 373–379.

[78] J. A. Leiro, M. H. Heinonen, T. Laiho, I. G. Batirev, *J. Electron Spectrosc. Relat. Phenom.* **2003**, *128*, 205–213.

[79] K. Artyushkova, S. Rojas-Carbonell, C. Santoro, E. Weiler, A. Serov, R. Awais, R. R. Gokhale, P. Atanassov, *ACS Appl. Energy Mater.* **2019**, *2*, 5406–5418.

[80] A. Bonakdarpour, M. Lefevre, R. Yang, F. Jaouen, T. Dahn, J.-P. Dodelet, J. R. Dahn, *Electrochem. Solid-State Lett.* **2008**, *11*, B105–B108.

[81] Y. Shao, J.-P. Dodelet, G. Wu, P. Zelenay, *Adv. Mater.* **2019**, *31*, 1807615.

[82] U. I. Kramm, A. Zana, T. Vosch, S. Fiechter, M. Arenz, D. Schmeißer, *J. Solid State Electrochem.* **2016**, *20*, 969–981.

[83] S. L. Gojkovic, S. Gupta, R. F. Savinell, *J. Electrochem. Soc.* **1998**, *145*, 3493–3499.

[84] A. Song, L. Cao, W. Yang, Y. Li, X. Qin, G. Shao, *ACS Sustainable Chem. Eng.* **2018**, *6*, 4890–4898.

[85] C.-T. Hsieh, W.-Y. Chen, Y.-S. Cheng, *Electrochim. Acta* **2010**, *55*, 5294–5300.

[86] C. H. Choi et al., *Energy Environ. Sci.* **2018**, *11*, 3176–3182.

[87] K. Kumar, L. Dubau, M. Mermoux, J. Li, A. Zitolo, J. Nelayah, F. Jaouen, F. Maillard, *Angew. Chem. Int. Ed.* **2019**, doi:10.1002/anie.201912451.

Declaration

I herewith declare that I have composed the present thesis myself and without use of any other than the cited sources and aids. Sentences or parts of sentences quoted literally are marked as such; other references with regard to the statement and scope are indicated by full details of the publications concerned. The thesis in the same or similar form has not been submitted to any examination body and has not been published. This thesis was not yet, even in part, used in another examination or as a course performance. Furthermore, I declare that the submitted written (bound) copies of the present thesis and the version submitted on a data carrier are consistent with each other in contents.

_____

Marius Gollasch, Oldenburg, 31.01.2020

7 Appendix

Table 7.1: Fitting parameters for high-resolution XP spectra analysis.

	Fitted Peak	Peak BE [eV]	FWHM [eV]
C	graphitic	284.5 ± 0.0	0.99 ± 0.03
	π-bound C_{ox}	285.7 ± 0.0	1.20 ± 0.07
	σ-bound C_{ox}	287.0 ± 0.0	1.35 ± 0.49
	satellite	290.3 ± 0.1	5.03 ± 0.52
	artifact	283.5 ± 0.0	0.48 ± 0.08
N	pyridinic	398.1 ± 0.0	1.42 ± 0.01
	$Me-N_x$	399.6 ± 0.0	1.42 ± 0.02
	pyrrolic	400.8 ± 0.0	1.42 ± 0.02
	graphitic	402.0 ± 0.0	1.42 ± 0.02
	satellite	404.0 ± 0.1	5.15 ± 0.47
O	O=C	531.0 ± 0.0	2.33 ± 0.04
	O-C	532.9 ± 0.0	2.34 ± 0.38
	satellite	537.1 ± 0.1	4.91 ± 0.16

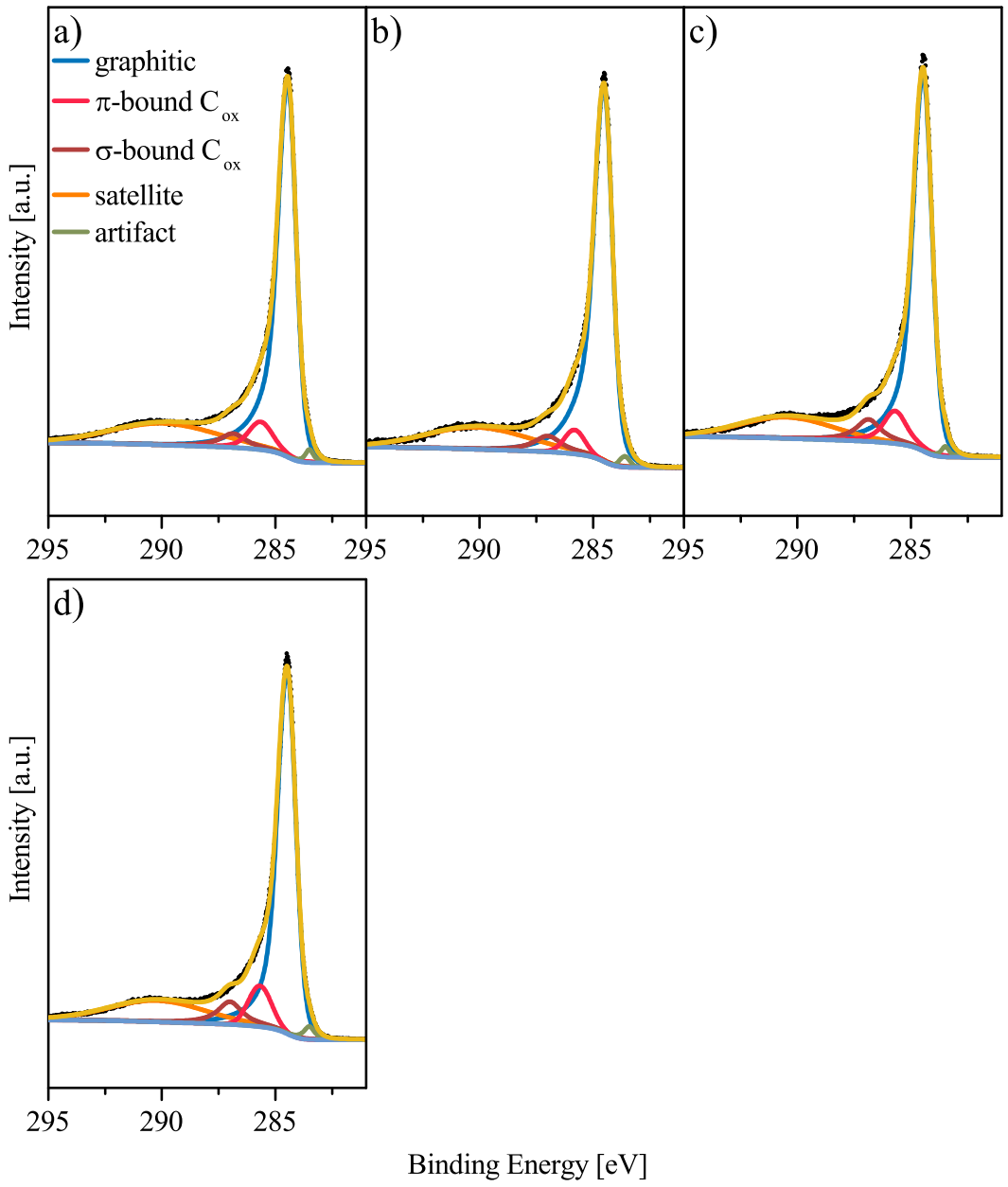

Figure 7.1: C1s high resolution XP spectra of a) FeCo-N-C (3:1), b) FeCo-N-C (5:3), c) FeCo-N-C (1:1) and d) FeCo-N-C (1:3).

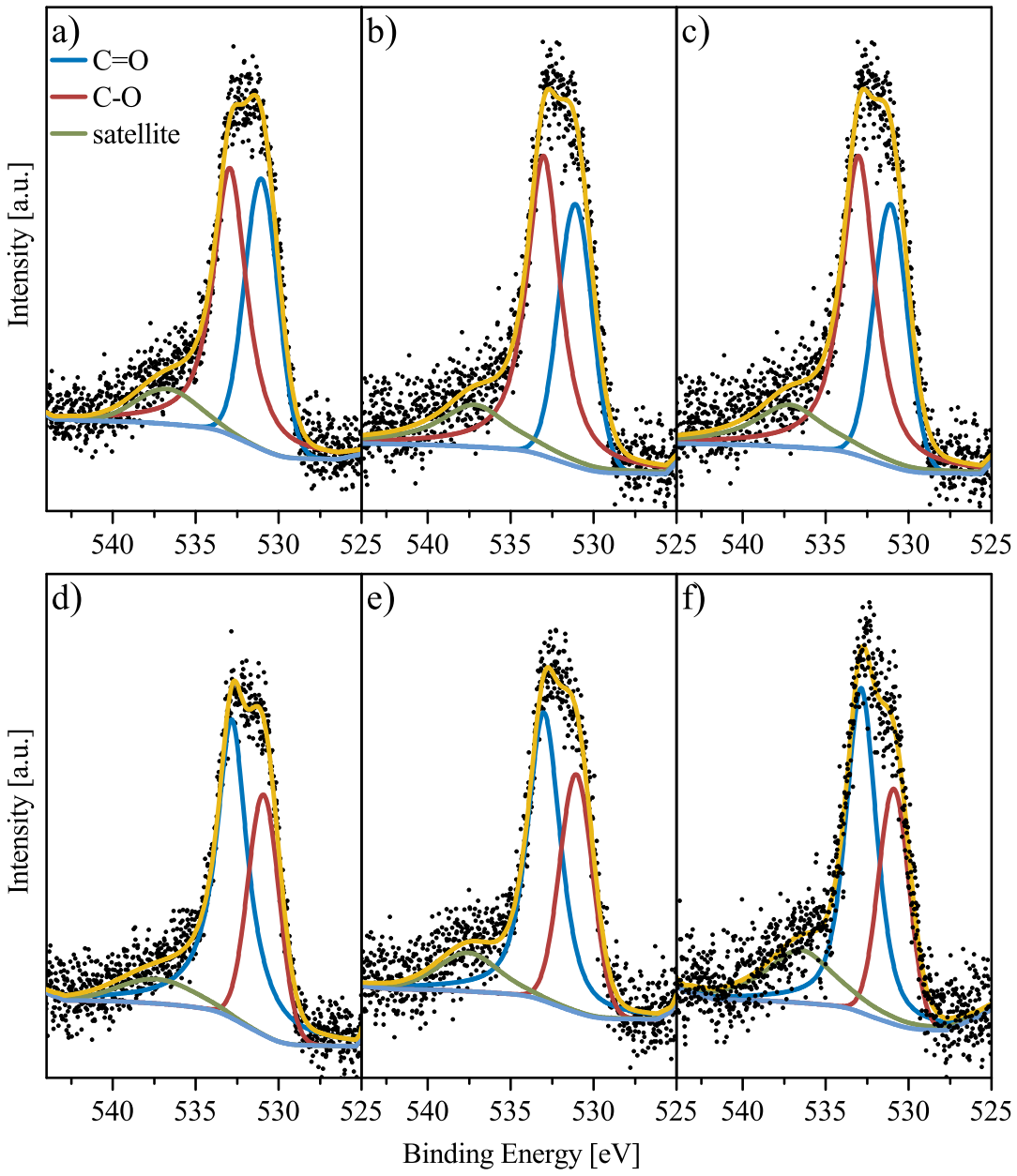

Figure 7.2: O1s high resolution XP spectra of a) Fe-N-C, b) FeCo-N-C (3:1), c) FeCo-N-C (5:3), d) FeCo-N-C (1:1), e) FeCo-N-C (1:3) and f) Co-N-C.

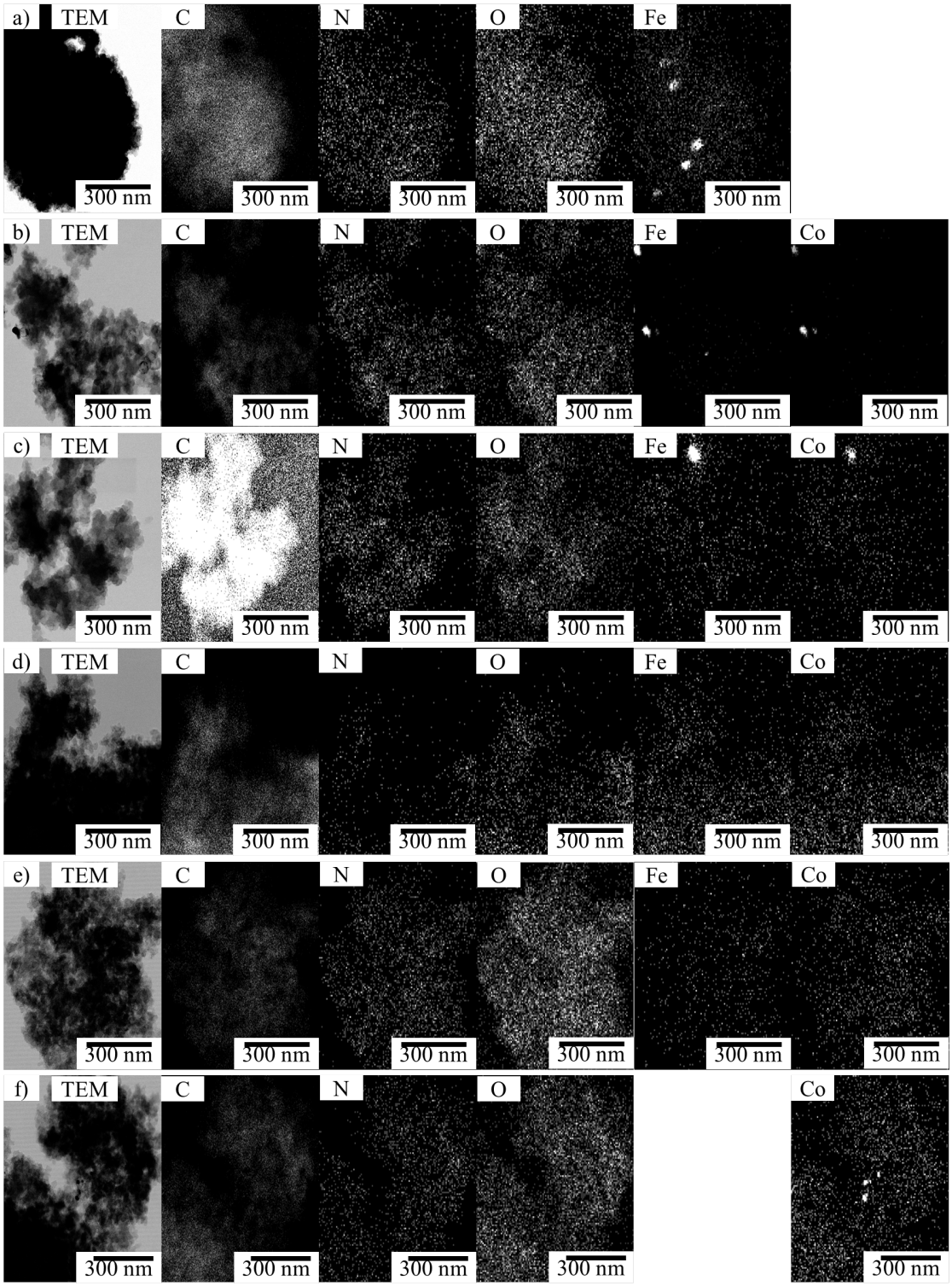

Figure 7.3: HR-TEM micrographs with EDS elemental mapping of a) Fe-N-C, b) FeCo-N-C (3:1), c) FeCo-N-C (5:3), d) FeCo-N-C (1:1), e) FeCo-N-C (1:3) and f) Co-N-C. C EDS mapping x2 amplified, other elements x4 amplified.